



L2hgdh Deficiency Accumulates L-2-Hydroxyglutarate with Progressive Leukoencephalopathy and Neurodegeneration

Shenghong Ma,^a Renqiang Sun,^a Bowen Jiang,^a Jun Gao,^{b,e} Wanglong Deng,^c Peng Liu,^a Ruoyu He,^d Jing Cui,^a Minbiao Ji,^d Wei Yi,^e Pengyuan Yang,^b Xiaohui Wu,^a Yue Xiong,^{a,f} Zilong Qiu,^g Dan Ye,^{a,h} Kun-Liang Guan^{a,i}

Molecular and Cell Biology Laboratory, Institute of Biomedical Sciences, Shanghai Medical College, Key Laboratory of Metabolism and Molecular Medicine, Ministry of Education, and Department of Biochemistry and Molecular Biology, School of Basic Medical Sciences, State Key Laboratory of Genetic Engineering and National Center for International Research of Development and Disease, Institute of Developmental Biology and Molecular Medicine, Collaborative Innovation Center of Genetics and Development, School of Life Sciences, Fudan University, Shanghai, China^a; Department of Chemistry & Institutes of Biomedical Sciences, Fudan University, Shanghai, China^b; State Key Laboratory of Medical Genomics and Shanghai Institute of Hematology, SJTU-SM, Shanghai, China^c; State Key Laboratory of Surface Physics and Department of Physics, Fudan University, Shanghai, China^d; China Novartis Institutes for BioMedical Research Co. Ltd., Shanghai, China^e; Lineberger Comprehensive Cancer Center, Department of Biochemistry and Biophysics, University of North Carolina at Chapel Hill, Chapel Hill, North Carolina, USA^f; Institute of Neuroscience, Key Laboratory of Primate Neurobiology, State Key Laboratory of Neuroscience, CAS Center for Excellence in Brain Science and Intelligence Technology, Shanghai Institutes for Biological Sciences, Chinese Academy of Sciences, Shanghai, China^g; Department of General Surgery, Huashan Hospital, Fudan University, Shanghai, China^h; Department of Pharmacology and Moores Cancer Center, University of California San Diego, La Jolla, California, USAⁱ

ABSTRACT L-2-Hydroxyglutarate aciduria (L-2-HGA) is an autosomal recessive neurometabolic disorder caused by a mutation in the L-2-hydroxyglutarate dehydrogenase (*L2HGDH*) gene. In this study, we generated *L2hgdh* knockout (KO) mice and observed a robust increase of L-2-hydroxyglutarate (L-2-HG) levels in multiple tissues. The highest levels of L-2-HG were observed in the brain and testis, with a corresponding increase in histone methylation in these tissues. *L2hgdh* KO mice exhibit white matter abnormalities, extensive gliosis, microglia-mediated neuroinflammation, and an expansion of oligodendrocyte progenitor cells (OPCs). Moreover, *L2hgdh* deficiency leads to impaired adult hippocampal neurogenesis and late-onset neurodegeneration in mouse brains. Our data provide *in vivo* evidence that *L2hgdh* mutation leads to L-2-HG accumulation, leukoencephalopathy, and neurodegeneration in mice, thereby offering new insights into the pathophysiology of L-2-HGA in humans.

KEYWORDS L2HGDH, 2-HG, leukoencephalopathy, gliosis, neurodegeneration

The rare, autosomal recessive neurometabolic disorders D-2-hydroxyglutaric aciduria (D-2-HGA) and L-2-hydroxyglutaric aciduria (L-2-HGA) are characterized by the accumulation of D-2-hydroxyglutarate (D-2-HG) and L-2-hydroxyglutarate (L-2-HG), respectively, in body fluids. Genetic characterization has shown that 50% of the D-2-HGA population and the majority of L-2-HGA patients harbor pathogenic mutations in *D2HGDH* and *L2HGDH* genes, respectively (1–3). The other half of D-2-HGA patients have a gain-of-function mutation in isocitrate dehydrogenase 2 (IDH2) at the residue of R140 (R140Q), which leads to abnormally high accumulation of D-2-HG (4). Based on phenotypic severity in patients, D-2-HGA is classified as mild type I (*D2HGDH* mutation) and severe type II (*IDH2* mutation) (4, 5). Of note, 2-HG concentrations are 2- to 8-fold higher for type II D-2-HGA than type I D-2-HGA patients (4, 6, 7), suggesting that

Received 5 September 2016 Returned for modification 4 November 2016 Accepted 24 January 2017

Accepted manuscript posted online 30 January 2017

Citation Ma S, Sun R, Jiang B, Gao J, Deng W, Liu P, He R, Cui J, Ji M, Yi W, Yang P, Wu X, Xiong Y, Qiu Z, Ye D, Guan K-L. 2017. *L2hgdh* deficiency accumulates L-2-hydroxyglutarate with progressive leukoencephalopathy and neurodegeneration. *Mol Cell Biol* 37:e00492-16. <https://doi.org/10.1128/MCB.00492-16>.

Copyright © 2017 American Society for Microbiology. All Rights Reserved.

Address correspondence to Zilong Qiu, zqiu@ion.ac.cn, or Dan Ye, [yedat@fudan.edu.cn](mailto:yedan@fudan.edu.cn).

endogenous D2HGDH is insufficient to metabolize the excessive D-2-HG produced by mutated IDH2. Compared to D-2-HGA, L-2-HGA is more prevalent and severe and mainly affects the central nervous system (CNS) starting at childhood, leading to progressive hypotonia, tremor, epilepsy, leukoencephalopathy, mental retardation, psychomotor regression, and low-frequency brain tumors (8–10). The neurological symptoms in L-2-HGA patients may be due to the toxicity from L-2-HG accumulation, although the underlying mechanisms are largely unclear.

Emerging evidence has indicated that mitochondrial dysfunction and impairment of oxidative phosphorylation (OXPHOS) are involved in the pathology of various organic acidemias. Recently, 2-HG has been reported to impair the activities of two enzymes in OXPHOS, including cytochrome *c* oxidase and ATP synthase (11, 12), but whether the pathogenesis of 2-HGA is associated with impairment of OXPHOS remains unknown. Furthermore, 2-HG is now considered an oncometabolite (13–16), and numerous studies indicate that altered epigenetic regulation is a major mechanism underlying its oncogenic activity. The structural similarity of 2-HG to α -ketoglutarate (α -KG) enables it to act as an α -KG analog and inhibit the activity of multiple α -KG-dependent dioxygenases, including the JmjC domain-containing histone demethylases and the TET (ten-eleven translocation) family of cytidine hydroxylases (13, 17–19). Supporting this notion, a mouse *Idh1-R132H* knock-in study reveals increases of both DNA and histone methylations (3). *In vitro* studies demonstrate that L-2-HG is more potent than D-2-HG in suppressing the activity of α -KG-dependent dioxygenases (13, 17).

Although it has been over 30 years since the first report of L-2-HGA, the progression of the disease is poorly understood and little is known about its long-term impact on neural development and neural activity (20). Recently, Rzem et al. constructed an *L2hgdh* deletion mouse model and found extensive vacuolations in the central nervous system (CNS) (21). To study the biochemical and pathophysiological consequences of L-2-HG accumulation, we created *L2hgdh* knockout (KO) mice by piggyBac transposon-mediated insertion mutation of the *L2hgdh* gene. Our data demonstrate an age-dependent accumulation of L-2-HG in the cerebrum and alterations in a subset of histone methylations in the CNS of *L2hgdh* KO mice. Importantly, *L2hgdh* KO mice exhibit subcortical white matter abnormalities, recapitulating the typical clinical features of L-2-HGA patients. Moreover, *L2hgdh* KO mice exhibit dys/demyelination, extensive gliosis, expanded cell numbers of oligodendrocyte progenitor cells (OPCs), and microglia-mediated neuroinflammation. Finally, *L2hgdh* KO mice also show impaired adult hippocampal neurogenesis as well as age-dependent neurodegeneration.

RESULTS

L2hgdh deficiency causes 2-HG accumulation, reduced body weight, and premature death in mice. To understand the pathophysiology of L-2-HGA, we generated an L-2-HGA mouse model in which the *L2hgdh* gene was disrupted by insertion of a piggyback (PB) transposon between exon 1 and exon 2 (see Fig. S1 in the supplemental material). Western blot analysis demonstrated expression of L2hgdh protein across diverse mouse tissues (Fig. S2). Heterozygous insertion of the PB transposon led to reduced L2hgdh protein expression, whereas homozygous insertion resulted in a complete loss of L2hgdh protein in a variety of mouse tissues tested (Fig. 1A), confirming the deletion and functional inactivation of the *L2hgdh* gene.

Measurement of 2-HG levels revealed that the urinary excretion of L-2-HG was approximately 6 to 8 mmol/mmol creatinine in *L2hgdh* KO mice, and that the plasma levels of L-2-HG were about 50 μ M (Fig. 1B and C). The L-2-HG concentrations in body fluids of *L2hgdh* KO mice were much higher than those of wild-type mice and were even comparable with those in L-2-HGA patients (2). Moreover, examination of L-2-HG in tissues of *L2hgdh* KO mice demonstrated that this metabolite was most abundant in the brain and testis, with L-2-HG concentrations of 4 mmol/kg tissue weight (Fig. 1D). In other tissues of *L2hgdh* KO mice, 2-HG was accumulated to a lesser extent, ranging from 40 μ mol/kg tissue weight in fat to 400 to 800 μ mol/kg tissue weight (Fig. 1D).

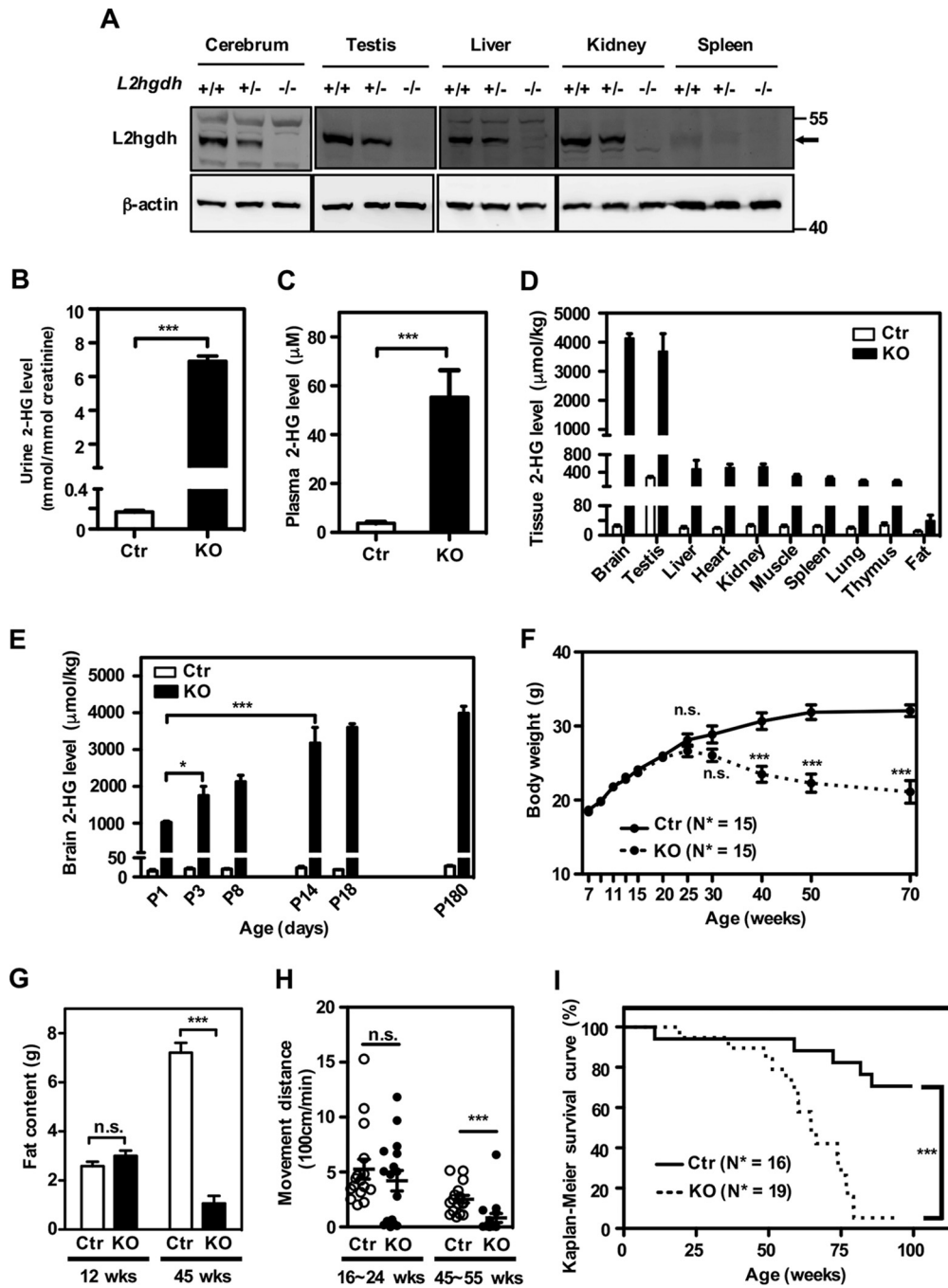


FIG 1 Deletion of *L2hgdh* leads to 2-HG accumulation, reduced body weight, and premature death in mice. (A) *L2hgdh* protein is diminished in *L2hgdh*^{-/-} mice. Western blotting of *L2hgdh* in tissues from cerebrium, testis, liver, kidney, and spleen of *L2hgdh* wild-type and piggyBac insertion heterozygous and homozygous mice. Beta-actin was used as a loading control (Ctr). (B and C) 2-HG is highly accumulated in urine (B) and plasma (C). 2-HG content in urine was measured by GC-MS and normalized to creatinine. (D) 2-HG accumulation in different tissues in *L2hgdh* KO mice. For each bar, tissues were collected from 3 or 4 mice at 2 to 3 months of age. (E) Temporal accumulation of 2-HG in postnatal mouse brains. Cerebral tissue at postnatal days 1, 3, 8, 14, 18, and 180 was collected for GC-MS analysis. (F) Age-dependent body weight loss in *L2hgdh* KO mice. For each time point and each genotype, *n* = 15. (G) Reduction of fat content in *L2hgdh* KO mice. Whole-body fat content was measured by a minispec (*n* = 8 to 10 per bar). (H) *L2hgdh* KO causes reduced locomotion in old mice. The open field test was applied to monitor mouse motor activity. Two age groups, 16 to 24 weeks and 45 to 55 weeks, were selected for testing. Each dot represents the movement of an individual mouse. (I) Premature death in *L2hgdh* KO mice. For wild-type and *L2hgdh* KO mice, *n* = 16 and 19, respectively. Quantifications are presented as means ± SEM and were analyzed by two-tailed *t* test. ***, *P* < 0.001; **, *P* < 0.01; *, *P* < 0.05; n.s., not significant.

Notably, we found an age-dependent increase of L-2-HG level in the cerebrum of postnatal *L2hgdh* KO mice (Fig. 1E). The L-2-HG level in the cerebrum was about 1 mmol/kg tissue weight at neonatal day 1, gradually increased to about 4 mmol/kg tissue weight at day 14, and thereafter was maintained at a high steady-state level (Fig. 1E). Neonatal *L2hgdh* KO mice exhibited no overt structural or cellular defects in the brain (data not shown).

Strikingly, *L2hgdh* KO but not wild-type mice older than 6 months exhibited a significant loss in body weight, decreasing by 30% in 1-year-old *L2hgdh* KO mice compared to wild-type controls (Fig. 1F). Time domain-nuclear magnetic resonance (TD-NMR) analysis revealed that loss of body weight was largely attributed to reduced fat content in older *L2hgdh* KO mice (Fig. 1G). Furthermore, the motor activity of *L2hgdh* KO mice and their wild-type littermates was evaluated with the open field test (OFT), and no difference in the moving distance was found between young *L2hgdh* KO mice and their wild-type littermates aged 16 to 24 weeks (Fig. 1H). In contrast, the distance moved by older *L2hgdh* KO mice was significantly decreased compared to that of their wild-type littermates aged 45 to 55 weeks (Fig. 1H). We also found that the majority of *L2hgdh* KO mice ($n = 18$ of 19) died at the age of 48 to 72 weeks (12 to 18 months), while most of the wild-type littermates were still alive at the same age (Fig. 1I). Collectively, these data indicate that deletion of *L2hgdh* leads to reduced motor activity, reduced body weight, and premature death in mice.

L2hgdh deficiency results in testicular atrophy and selective changes in histone methylation. Our observation that L-2-HG was most abundant in the testis and brain of *L2hgdh* KO mice (Fig. 1D) prompted us to examine the pathophysiological consequences of L-2-HG accumulation in these two tissue types. We found that *L2hgdh* KO mice exhibited testicular atrophy and that this phenotype was exacerbated at an advanced age (Fig. 2A and B). Histological analysis showed that the seminiferous tubules had normal anatomy and spermatogenesis in *L2hgdh* KO mice compared to the wild-type controls (Fig. 2C). *L2hgdh* KO male mice were fertile but less potent than their wild-type littermates (data not shown). Together, these data indicate that *L2hgdh* deficiency and high L-2-HG accumulation affect the organ size but not the development of the testis.

It is known that 2-HG acts as an α -KG antagonist to inhibit the activity of α -KG-dependent dioxygenases, including the JmjC domain-containing histone demethylases and the TET family of DNA cytidine hydroxylases (17, 22). We therefore performed multiple reaction monitoring (MRM) based on liquid chromatography-tandem mass spectrometry (LC-MS/MS) analysis with isotopically labeled standards to quantify relative histone levels (23, 24). Our data revealed that H3K9me2 and H3K9me3 levels were significantly increased while H3K9me0 levels were reduced in the testis of *L2hgdh* KO mice (Fig. 2D). In addition, H3K27me2 levels significantly increased while H3K27me0 levels decreased moderately in the testis of *L2hgdh* KO mice (Fig. 2D). In contrast, other histone methylation markers, including H3K4me1/2/3 and H3K79me1/2/3, were not substantially changed in the testis of *L2hgdh* KO mice (Fig. 2D).

The effects of *L2hgdh* deficiency and L-2-HG accumulation on histone methylation markers was also observed in the brain, where L-2-HG accumulation is the highest (Fig. 1D). We found that H3K9me2 was significantly increased while the H3K9me0 level was reduced in the cerebrum of *L2hgdh* KO mice (Fig. 2E). As a result, the H3K9me2/H3K9me0 ratio increased by 37% in the cerebrum of *L2hgdh* KO mice compared to wild-type littermates. Moreover, H3K27me3 was significantly increased, and the H3K27me2 level accordingly was reduced in the cerebrum of *L2hgdh* KO mice (Fig. 2E). Furthermore, H3K36me2 increased significantly in the cerebrum of *L2hgdh* KO mice (Fig. 2E). In contrast, other histone methylation markers were not substantially altered in the cerebrum of *L2hgdh* KO mice, including H3K4me1/2/3 and H3K79me1/2/3 (Fig. 2E). *L2hgdh* deficiency had no effect on histone methylation in other tissues that showed only moderate accumulation of L-2-HG, such as the liver, kidney, and heart (Fig. S3A to C). Collectively, these findings suggest that *L2hgdh* deficiency leads to

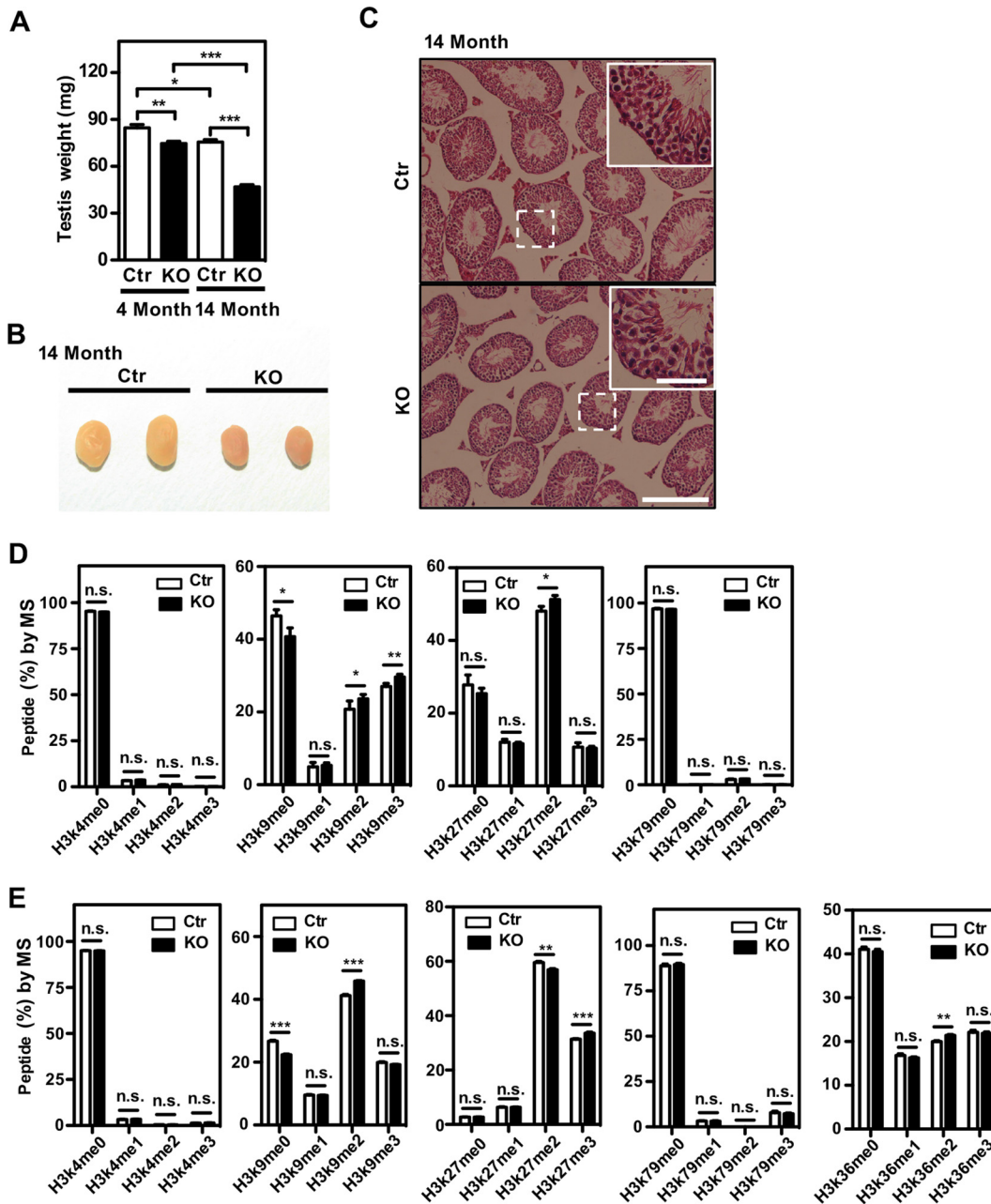


FIG 2 Testis atrophy and increased histone lysine methylation in *L2hgdh* KO mice. (A) Age-dependent testis atrophy in wild-type (Ctrl) and *L2hgdh* KO mice. (B) Representative testes from *L2hgdh* KO mice and wild-type littermates at postnatal month 14. (C) HE staining of representative testis morphology at postnatal month 14. Scale bars at the lower and upper right are 200 μ m and 50 μ m, respectively. (D and E) Analysis of histone methylation of the testis (D) and cerebrum (E). Histone methylation on K4, K9, K27, K36, and K79 was determined and is presented. Quantification of histone modification was calculated from five independent samples and is presented as means \pm SEM; data were analyzed by a two-tailed *t* test. ***, $P < 0.001$; **, $P < 0.01$; *, $P < 0.05$; n.s., not significant.

changes in a subset of histone methylation markers in mouse testis and brain, where L-2-HG accumulation is the highest.

Besides histone demethylases, the TET family of DNA hydroxylases is another major pathologically relevant target of 2-HG (13, 25). TET enzymes catalyze three sequential oxidative reactions, converting 5-methylcytosine (5mC) first to 5-hydroxymethylcytosine (5hmC), then to 5-formylcytosine (5fC), and finally to 5-carboxylcytosine (5caC) (26–28). We next performed LC-MS analysis to measure and quantify 5mC and its oxidative derivatives in the cerebrum of *L2hgdh* KO mice and wild-type littermates. Our data demonstrated that

L2hgdh deficiency and high accumulation of L-2-HG had a minor effect on the genomic levels of 5mC/5hmC/5fC in the cerebrum of *L2hgdh* KO mice (Fig. S4A to C). Previously, it was reported in an *Idh1* mutant knock-in mouse model that accumulated D-2-HG in the brain was associated with reduced hydroxylation of hypoxia-inducible transcription factor 1 alpha (Hif-1 α) as well as collagen type IV, leading to endoplasmic reticulum (ER) stress response, blood-brain barrier aberration, and hemorrhage (29). However, no sign of hemorrhage was found in the cerebrum of *L2hgdh* KO mice (data not shown). Furthermore, the levels of Hif-1 α protein or eukaryotic initiation factor 2 α (eIF2 α) phosphorylation were not altered in the cerebrum of *L2hgdh* KO mice compared to their wild-type littermates (Fig. S4D). Moreover, the blood vessel distribution of collagen type IV was intense and continuous in the cerebrum of *L2hgdh* KO mice (Fig. S4E and data not shown), implying that hydroxylation modification and maturation of collagens are not disturbed by *L2hgdh* deficiency and L-2-HG accumulation.

L2hgdh deficiency leads to early-onset white matter abnormality. MRI (magnetic resonance imaging) analysis from previous reports suggest that the pathological changes in L-2-HGA patients are abnormalities of the subcortical cerebral white matter dentate nucleus, globus pallidus, putamen, and caudate nucleus (30). Using T2-weighted MRI analysis, we found that the signal intensity of the subcortical corpus callosum (cc) and striatum was consistently increased in *L2hgdh* KO mice compared to wild-type littermates (Fig. 3A). *L2hgdh* KO mice therefore display white matter abnormalities similar to those observed in L-2-HGA patients.

Changes of MRI signal intensity normally reflect alterations in chemical composition. Therefore, we used stimulated Raman scattering (SRS) microscopy to analyze the chemical composition of our biological samples (31, 32). While protein signal intensity did not change in the striatum of *L2hgdh* KO mice, lipid signal intensity was remarkably weakened in the white matter fiber of the striatum as well as corpus callosum in *L2hgdh* KO mice compared to wild-type littermates (Fig. 3B and data not shown). Since the white matter fiber of the striatum is mainly composed of axons and the surrounding myelin, we hypothesized that *L2hgdh* deficiency leads to widespread dys/demyelination in the brain. Supporting this notion, Luxol fast blue (LFB) staining of mouse brain cryosections revealed that the content of myelin was dramatically reduced in the cerebrum of *L2hgdh* KO mice, including the cortex, corpus callosum, and striatum (Fig. 3C). Likewise, FluoroMyelin staining showed significantly reduced lipid signal in the white matter fiber of the striatum as well as the corpus callosum in *L2hgdh* KO mice (Fig. 3D and data not shown). Consistent with this finding, the total protein level of MBP (myelin basic protein) was reduced by 60% in the cerebrum of *L2hgdh* KO mice compared to wild-type littermates (Fig. 3E and F). Furthermore, transmission electron microscopy (TEM) analysis showed reduced myelination intensity and naked axons in the white matter fibers of the striatum in *L2hgdh* KO mice (Fig. 3G). Together, these results suggest that *L2hgdh* deficiency leads to widespread dys/demyelination in mouse brain.

To determine the time point when dys/demyelination initially occurred, we utilized SRS microscopy to examine cryosections of mouse brains at different ages. We found that the lipid signal intensity was comparable between *L2hgdh* KO mice and wild-type littermates at postnatal day 9 (p9) and that the lipid signal intensity thereafter was gradually increased in wild-type mice but much more stagnant in *L2hgdh* KO mice (Fig. 3H). As a result, an obvious reduction in lipid signal intensity was detected in *L2hgdh* KO mice as early as postnatal day 12 (Fig. 3H).

To determine whether L-2-HG accumulation in *L2hgdh* KO mice impairs OPC myelination and early differentiation to oligodendrocytes, we isolated and cultured OPCs from the cerebral tissue of KO and control mice at postnatal day 7. The isolated OPCs were of high purity, as greater than 90% stained positive for the OPC marker NG2 (Fig. S5A). Early differentiation of *L2hgdh* KO OPCs induced by thyroid hormone T3 was unimpaired *in vitro* (Fig. S5B), indicating that L-2-HG affects later stages of OPC differentiation and myelination.

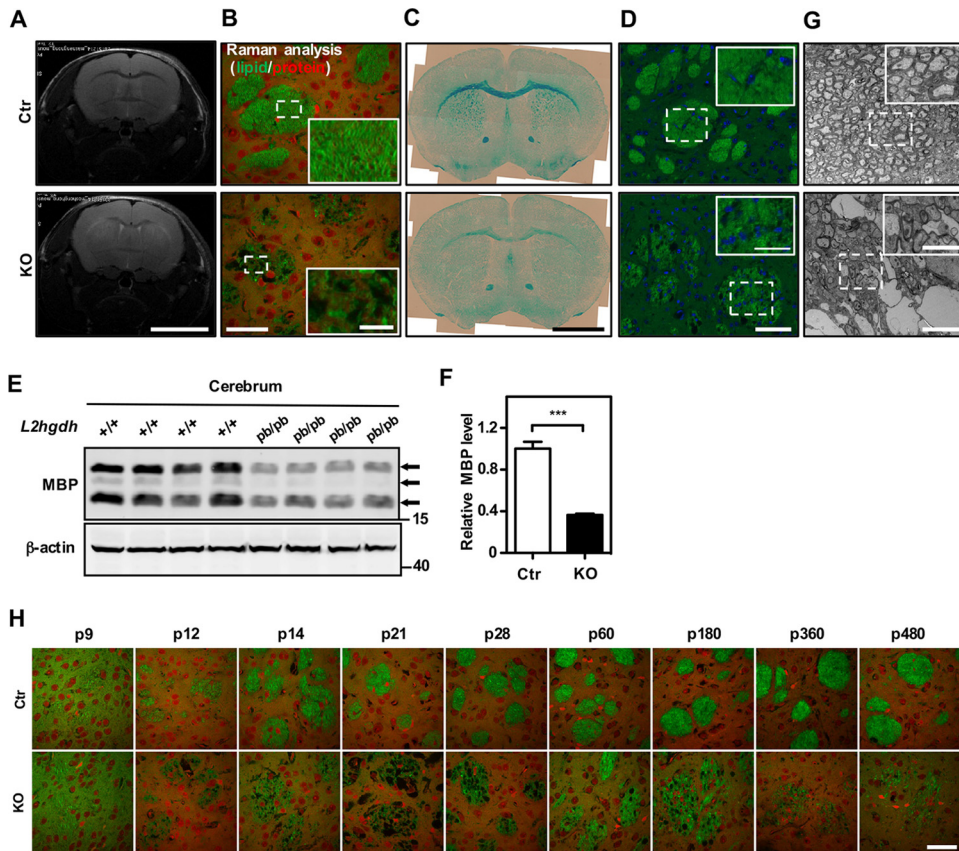


FIG 3 Deletion of *L2hgdh* leads to early-onset white matter abnormality and demyelination. (A) T2-weighted MRI. Hyperintense signals appeared in the external capsule and striatum in a coronal brain section of *L2hgdh* KO mice. The scale bar is 4 mm. (B) SRS microscopy showed a decreased lipid signal in the myelin fibers in the striatum of *L2hgdh* KO mice. Lipid and protein signals are represented as green and red, respectively. Scale bars at the lower left and right are 50 μm and 10 μm , respectively. (C) Luxol fast blue imaging of a whole coronal section showed reduced signal intensity in *L2hgdh* KO mice. The scale bar is 2 mm. (D) *L2hgdh* KO mice showed decreased FluoroMyelin staining in the myelin fibers of the striatum. Scale bars at the lower and upper right are 50 μm and 25 μm , respectively. (E and F) Western blotting of cerebrium samples for MBP (E) and quantification of results (F). ***, $P < 0.0001$. pb/pb, homozygous piggyback transposon insertion into the *L2hgdh* gene, equal to KO. (G) Transmission electron micrographs (TEM) of the myelin fibers in the striatum showed reduced myelination, naked axons, and vacuolation in *L2hgdh* KO mice. Mice aged 2 to 6 months were selected, and a representative image at 2 months is shown. Scale bars at the lower and upper right are 4 μm and 2 μm . (H) SRS microscopy for the myelin fibers of the striatum at postnatal ages p9, p12, p14, p21, p28, p60, p180, p360, and p480. The scale bar is 50 μm .

Besides dys/demyelination, an extensive spongiotic appearance was observed in multiple brain regions in *L2hgdh* KO mice, such as the brainstem, the basal ganglia (including the striatum), corpus callosum, hippocampus, inner layer of cortex, and cerebellar nucleus (Fig. S6). The appearance of vacuoles in the brainstem of *L2hgdh* KO mice was initially observed at postnatal day 8 and reached peak levels at the age of 2.5 to 3 weeks before gradually declining (Fig. S7A). This dynamic change in vacuolation was found in most of the examined brain regions with a close initiation time between postnatal days 8 and 11, with the exception being the dentate gyrus (DG) of the hippocampus, where a large vacuole was first observed in 1-year-old *L2hgdh* KO mice and became extremely severe thereafter (Fig. S7B).

L2hgdh deficiency leads to extensive gliosis. Approximately half of L-2-HGA patients show macrocephaly (2). Consistent with this report, we observed that the net brain weight was significantly increased in *L2hgdh* KO mice compared to wild-type littermates above 1 year of age (Fig. 4A and B). Measurements of cerebral cortical surface area revealed a 20 to 25% increase in *L2hgdh* KO mice compared to wild-type littermates (Fig. 4D), with a 15 to 20% reduction in cerebellum surface area in *L2hgdh*

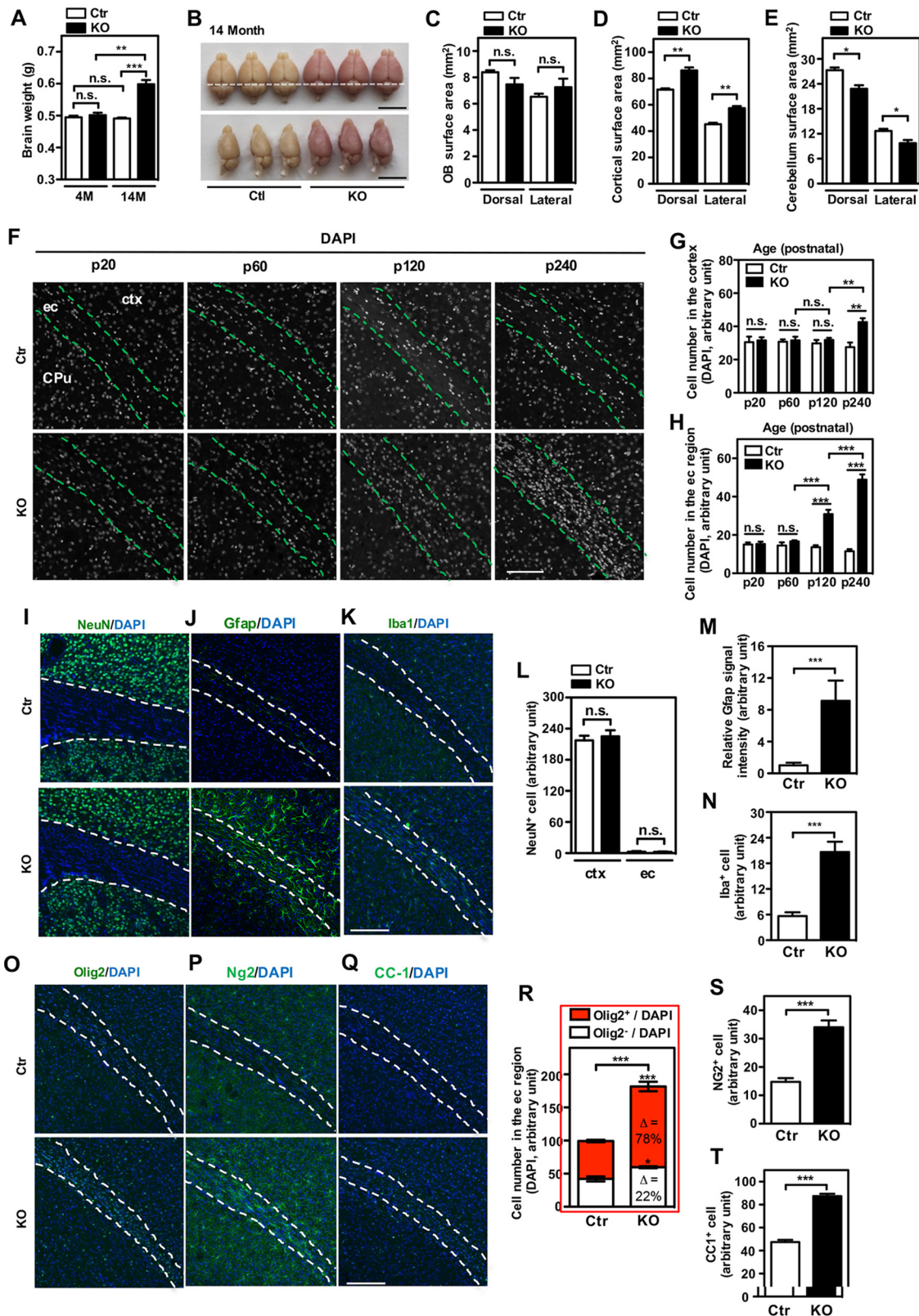


FIG 4 Deletion of *L2hgdh* increases glial cells and brain mass. (A) *L2hgdh* KO mice show increased brain weight at 14 months but not 4 months compared to their wild-type controls. Note that *L2hgdh* KO mice express RFP and have a red color due to the inserted transposon construct. For each group, *n* = 3. (B to E) Whole-mount images (B) and size quantification for OB (C), cerebrum (D), and cerebellum (E) of 14-month-old *L2hgdh* KO mice compared to their wild-type controls. For each group, *n* = 3. The scale bars are 1 cm. (F to H) Age-dependent increase in nuclear number in *L2hgdh* KO mice and quantification in the VI layer of primary somatosensory cortex (G) and the external capsule (H). DAPI was used for nuclear staining. ec, external capsule; CPu, striatum; ctx, cortex. The scale

(Continued on next page)

KO mice (Fig. 4E). In contrast, the surface area of olfactory bulbs (OB) was unchanged in *L2hgdh* KO mice compared to the wild-type controls (Fig. 4C). Notably, 4',6-diamidino-2-phenylindole (DAPI) staining for DNA revealed that the number of nuclei increased in the cerebrum of *L2hgdh* KO mice in an age-dependent manner (Fig. 4F). To confirm this observation, we quantified the number of nuclei in layer IV of the primary somatosensory cortex and beneath the external corpus in the brains of *L2hgdh* KO and wild-type littermates at different ages. There were no differences in the number of nuclei in the cortex or external corpus regions between *L2hgdh* KO mice and wild-type littermates at postnatal day 20 or 60 (Fig. 4G and H). Strikingly, the number of nuclei in the cortex and external corpus increased significantly (by 35 to 45% and 3.5- to 4.5-fold, respectively) in *L2hgdh* KO mice compared to wild-type littermates at postnatal day 240. Actually, a 2- to 2.5-fold increase in nuclear number was observed even earlier in the external corpus of *L2hgdh* KO mice at postnatal day 120 (Fig. 4H). Together, these findings suggest that *L2hgdh* deficiency leads to an age-dependent increase in cell number in the cerebrum, which may contribute at least in part to macrocephaly.

The CNS is composed of diverse cell types, including neurons, astrocytes, oligodendrocytes and their progenitor cells (OPCs), and microglia. To identify the cell type(s) responsible for increased nuclear number in the cerebrum of *L2hgdh* KO mice, coronal sections of mouse brains were immunostained with different cell-type-specific markers. Neurons are the major cell type in the CNS and account for about two-thirds of the total cell population in the adult mouse brain. We found that NeuN⁺ cells were barely detectable in the external corpus of *L2hgdh* KO mice or wild-type littermates (Fig. 4I). No differences in NeuN⁺ cell number were observed in the cortex between *L2hgdh* KO mice and wild-type littermates (Fig. 4L), suggesting that neurogenesis in the cerebrum, which mostly occurs in the embryonic stage, is not disturbed. In contrast, Gfap (an astrocyte activation marker) dramatically increased in several regions of the cerebrum in *L2hgdh* KO mice older than 4 weeks, including the inner layer cortex, white matter, and striatum (Fig. 4J, M, and data not shown). Consistent with this, quantitative reverse transcription-PCR (qRT-PCR) analysis showed that Gfap mRNA levels increased 2.5- to 3-fold in the cerebrum of *L2hgdh* KO mice compared to wild-type littermates, while that of *Aldh111*, another astrocyte marker, was unchanged (Fig. S8), suggesting that *L2hgdh* deficiency and L-2-HG accumulation lead to activation but not increased proliferation of astrocytes in mouse brain. Astrocyte activation is often concomitant with the activation of microglia, which are considered resident macrophage cells and act as the first line of innate immune defense in the CNS. Indeed, we found that Iba1⁺ cells increased by 3-fold in the external corpus of *L2hgdh* KO mice at postnatal day 120 (Fig. 4K and N). In addition, the population of Olig2-positive cells (an oligodendrocyte lineage marker) increased by 2-fold and accounted for ~78% of all cells in *L2hgdh* KO mice at p120 (Fig. 4O and R). These data indicate that the expansion of oligodendrocyte lineage cells is a major contributor to increased nuclear number in *L2hgdh* KO mice. The oligodendrocyte lineage is comprised of OPCs. We found that the levels of Ng2-positive oligodendrocytes and CC1-positive OPCs were increased by 2- to 2.5-fold and 1.5- to 2-fold, respectively, in the external corpus of *L2hgdh* KO mice (Fig. 4P, Q, S, and T).

OPCs have been proposed to be the origin of gliomas (33, 34). The observed OPC expansion in the cerebrum of adult *L2hgdh* KO mice prompted us to investigate the oncogenic effect of *L2hgdh* deficiency and L-2-HG accumulation in the CNS. IDH1 mutant gliomas, which exhibit high levels of D-2-HG, often contain mutations in p53 (35, 36). We therefore crossed *L2hgdh* KO mice with *p53* KO mice and found that *L2hgdh*

FIG 4 Legend (Continued)

bar is 100 μm . (I to N) Increase in nuclear number was accompanied by reactive astrocytes and an increase in microglia but not neurons. Reactive astrocytes are represented by upregulation of Gfap in *L2hgdh* KO mice (J), and the quantification is shown (M). NeuN (I and L) and Iba1 (K and N) are representative markers for microglia and neurons, respectively. The scale bar for panels I to K is 200 μm . (O to Q) Immunostaining with oligodendrocyte lineage cell marker Olig2 (O), OPC cell marker NG2 (P), and mature oligodendrocyte marker cc-1 (Q), which is quantified in panels R to T. The scale bar for panels I to K is 200 μm . Quantifications are presented as means \pm SEM and were analyzed by two-tailed *t* test. ***, $P < 0.001$; **, $P < 0.01$; *, $P < 0.05$; n.s., not significant.

and *p53* double KO mice developed tumor types similar to those of *p53* single KO mice, most of which were lymphoma and peripheral tumors but not brain tumors (data not shown). Notably, deletion of both *L2hgdh* and *p53* genes did not significantly change tumor-free survival in mice compared to the single *p53* deletion controls (Fig. S9). A likely explanation is that the *p53* deletion produces a very strong tumor phenotype, which may mask the effect of *L2hgdh* deficiency on tumorigenesis. Together, our data suggest that *L2hgdh* deficiency and L-2-HG accumulation lead to an increased glial population and a neoplastic state via the expansion of OPC; however, deletion of *L2hgdh* does not induce an overtly malignant phenotype in mouse brains either alone or in combination with whole-body *p53* deletion.

L2hgdh deficiency results in reactive gliosis and neuroinflammation. As shown earlier in this study, a subset of histones showed increased methylation in the CNS of *L2hgdh* KO mice (Fig. 2E). Histone methylation not only affects chromatin status and transcription factor recruitment to regulate gene expression (37) but also has been linked to a number of neurological and psychiatric disorders (38). This prompted us to perform RNA-sequencing experiments in hippocampal tissue of mice at the age of postnatal day 60, when glial cell numbers have not yet increased. Surprisingly, there were only selective groups of genes whose transcriptional expression was different in the hippocampus of *L2hgdh* KO mice compared to wild-type littermates (Fig. 5A and B). For instance, the gene ontology (GO) item “oxidation reduction” is the top dysregulated pathway in the *L2hgdh* KO mice compared to wild-type littermates (Fig. 5C). In accordance with this, we found that the level of glutathione (GSH) was significantly reduced by 30% in the cerebrum of *L2hgdh* KO mice (Fig. 5D). In agreement with our histological findings (Fig. 3 and 4), we detected significant dysregulation of GO items involved in myelination, axon ensheathment, and cell proliferation in *L2hgdh* KO mice (Fig. 5C). In addition, genes involved in “immune response” and “chemotaxis” were also dysregulated (Fig. 5C). To verify the RNA-sequencing data, we performed qRT-PCR analysis and found that multiple genes involved in chemotaxis and immune response were indeed upregulated in the cerebrum of *L2hgdh* KO mice, including *Clec7a*, *Itgax*, *Cybb*, *Tnf*, and *Ccl* family genes *Ccl3/4/6* but not *Ccl2/5* (Fig. 5E). When mouse brain tissues were immunostained with Cd3 and Mpo (lymphocyte and neutrophil markers, respectively), we found that neither Cd3⁺ nor Mpo⁺ cells could be detected in the cerebrum of *L2hgdh* KO mice or wild-type littermates (Fig. S10). This indicated that the observed immune response triggered by chemotaxis in the cerebrum of *L2hgdh* KO mice is not caused by peripheral lymphocyte or neutrophil infiltration into the CNS. It should be noted that genes involved in the pathways of chemotaxis and immune response are predominantly expressed in microglia in the CNS (Fig. S11). Immunofluorescence staining demonstrated that the signal intensity of Cd68 was significantly upregulated in the cerebrum of *L2hgdh* KO mice at postnatal day 60 and strongly overlapped with microglia-specific marker Iba1 (Fig. 5F), indicating that the elevated immune response is mediated by microglia. Our data therefore suggest that *L2hgdh* deficiency leads to microglia activation prior to cell number proliferation in the adult mouse brain.

L2hgdh deficiency results in impaired adult hippocampal neurogenesis and late-onset neurodegeneration. We next investigated the impact of *L2hgdh* deletion and 2-HG accumulation on neurons, the major cell type in the CNS. Continuous neurogenesis throughout life occurs primarily in the subventricular zone of the lateral ventricles (SVZ) as well as the subgranular zone (SGZ) of the DG in the hippocampus. Notably, we found that the number of cells which were positive for nestin, a specific marker for neural progenitor cells (NPCs), decreased by 80% in the SGZ of 8-week-old *L2hgdh* KO mice compared to that in wild-type controls (Fig. 6A and B), suggesting that *L2hgdh* is important for maintaining the NPC pool in the hippocampal SGZ of the adult mouse brain. In addition, we also used specific cell lineage markers to test the effect of *L2hgdh* KO on the population of nonradial progenitor cells and newborn neurons. Immunofluorescence staining illustrated that the number of Tbr2-positive nonradial

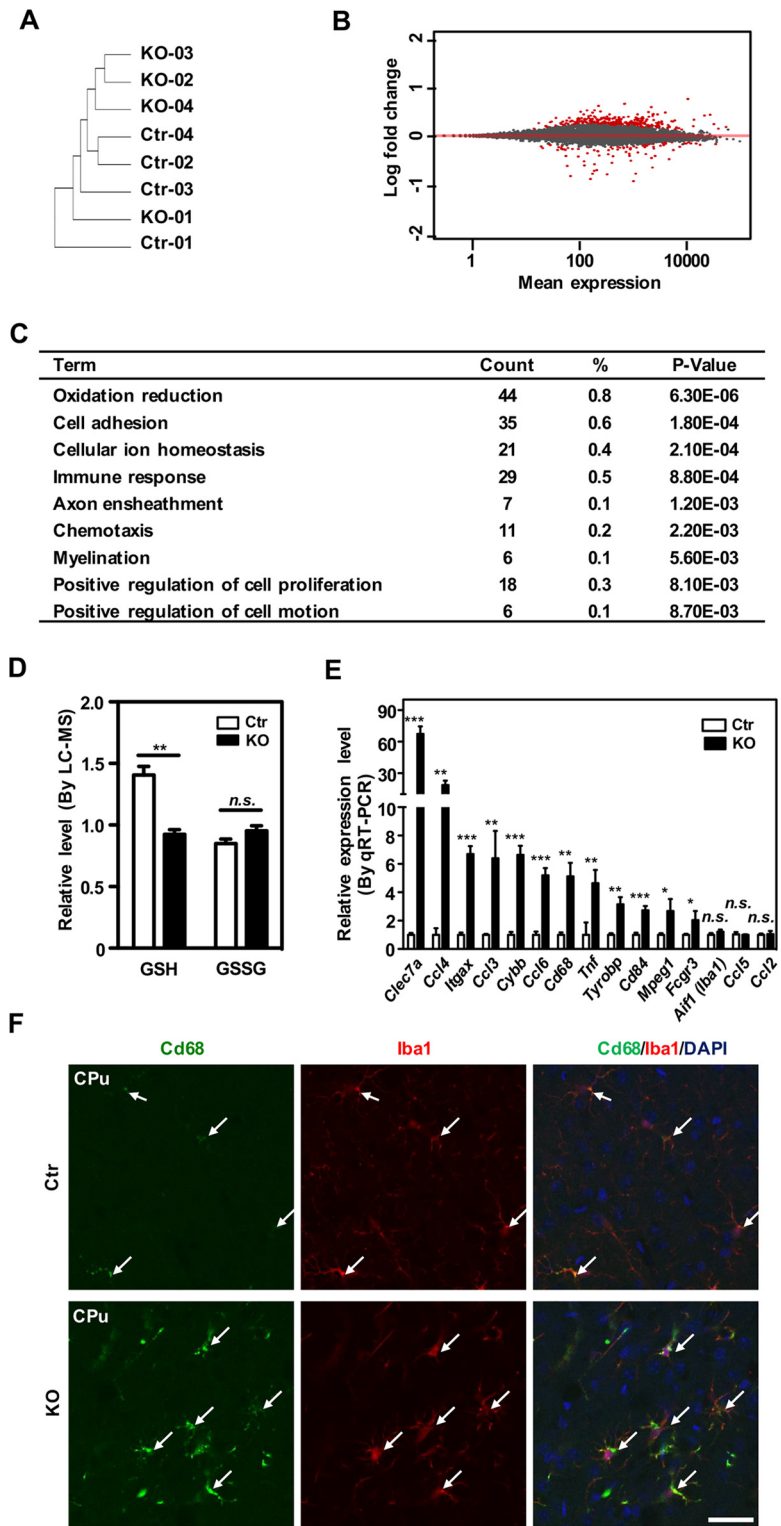


FIG 5 Deletion of *L2hgdh* results in disturbed redox status and neuroinflammation. (A) Gene expression profiling and clustering analysis of the hippocampus of *L2hgdh* KO mice and their wild-type controls. (B) MA plot of differential gene expression in the brains of *L2hgdh* KO and wild-type mice. The horizontal axis represents gene expression levels (FPKM), while the vertical axis represents relative fold changes in gene expression between *L2hgdh* KO and wild-type mice. Each dot represents one gene, and red dots indicate genes with differential expression using a cutoff (*q* value) of <0.1 (Benjamini-Hochberg method or false discovery rate). (C) Gene ontology (GO) analysis of differentially expressed genes. (D) *L2hgdh* KO reduces GSH levels in the cerebrum. Whole-cerebrum tissues of adult *L2hgdh* KO and wild-type mice were used for LC-MS/MS to measure GSH and GSSG levels. Three mice were used for each group. (E) qRT-PCR

(Continued on next page)

progenitor cells decreased by 70% in the SGZ of 8-week-old *L2hgdh* KO mice (Fig. 6C and D). Moreover, *Dcx*-positive newborn neurons were reduced by 60 to 70% in the same brain region in *L2hgdh* KO mice (Fig. 6E and F and Fig. S12). Together, these results provide *in vivo* evidence that adult hippocampal neurogenesis is impaired in *L2hgdh* KO mice.

Furthermore, we analyzed NPCs isolated from neonatal mouse hippocampus and found that *L2hgdh*-deficient NPCs showed lower proliferation capacity than the wild-type controls (Fig. 6G). To determine the self-renewal capacity of these NPCs, primary neurospheres were individually dissociated into single cells and replated at clonal density for three additional passages. This replating assay revealed that *L2hgdh*-deficient NPCs also exhibited lower capacity for self-renewal (Fig. 6G). However, we found that the differentiation potential of NPCs was not affected by *L2hgdh* deletion (Fig. 6H to J). Upon differentiation *in vitro*, the neurospheres from *L2hgdh* KO mice were tripotent, with comparable abilities to generate neurons, astrocytes, and oligodendrocytes as evidenced by immunostaining of *Tuj1*, *Gfap*, and *O4* markers, respectively (Fig. 6H to J). Thus, these data provide evidence that *L2hgdh* deficiency reduces the self-renewal capability of NPCs, thereby contributing to the impaired adult hippocampal neurogenesis in *L2hgdh* KO mice.

Reactive gliosis and neuroinflammation could be strong driving forces to facilitate neurodegeneration (39, 40). To examine neurodegeneration in *L2hgdh* KO mice, we performed Fluoro Jade-C (FJC) staining, which is widely used to label degenerating neurons (41). The number of FJC-positive cells increased remarkably in the cerebrum, especially the basal ganglia regions, including the globus pallidus and striatum, of 14-month-old *L2hgdh* KO mice compared to the wild-type controls (Fig. 6K and O and data not shown). In accordance with this, terminal deoxynucleotidyltransferase-mediated dUTP-biotin nick end labeling (TUNEL)-positive and cleaved caspase 3-positive signals were much stronger in the cerebrum of 14-month-old *L2hgdh* KO mice than in wild-type littermates (Fig. 6L, M, P, and Q), indicating that apoptosis is highly elevated in *L2hgdh*-deficient mouse brains.

DISCUSSION

In this study, we provide *in vivo* evidence that mutation of the detoxification enzyme *L2hgdh*, likely due to L-2-HG accumulation, causes abnormal myelination, disturbed glia/adult neural stem cell homeostasis, and increased cell death in the central nervous system. The major findings of this study, as summarized in Fig. 7, are as follows. Deletion of the *L2hgdh* gene leads to a time-dependent accumulation of the enzyme's substrate, L-2-HG, from $\sim 30 \mu\text{M}$ in control mouse tissues up to $4,000 \mu\text{M}$ in brain and testis, whereas most other tissues accumulate L-2-HG to $\sim 500 \mu\text{M}$. The earliest lesions in the central nervous system, which begin at postnatal week 2, include dysmyelination and vacuolation and are mainly but not exclusively myelin-rich regions of the corpus callosum (cc) and striatum fibers. In the dentate gyrus (DG), vacuoles are initially formed at 1 year of age but are exacerbated with age. The temporal heterogeneity of vacuolation suggests that there is more than one mechanism contributing to vacuolation in different brain regions. Gliosis represented by neuroinflammation of microglia and astrocyte activation starts as early as week 3 to 4. The neuroinflammation of microglia is strongly associated with the vacuolation (except in the DG), as both phenotypes decrease with time. *L2hgdh* deletion also increases the adult glial cell population, including oligodendrocytes, OPCs, and microglia. The increased number of oligodendrocytes, possibly from increased proliferation and differentiation of progenitor OPCs,

FIG 5 Legend (Continued)

verification of differentially expressed genes categorized as the GO items "chemotaxis" and "immune response." (F) Cd68 signal is upregulated in 2-month-old *L2hgdh* KO mice. Coimmunofluorescence of Cd68 and microglial marker *Iba1* shows highly overlapped staining. Representative images were taken in the striatum. The scale bar is $30 \mu\text{m}$. Quantifications are presented as means \pm SEM and were analyzed by two-tailed *t* test. ***, $P < 0.001$; **, $P < 0.01$; *, $P < 0.05$; n.s., not significant.

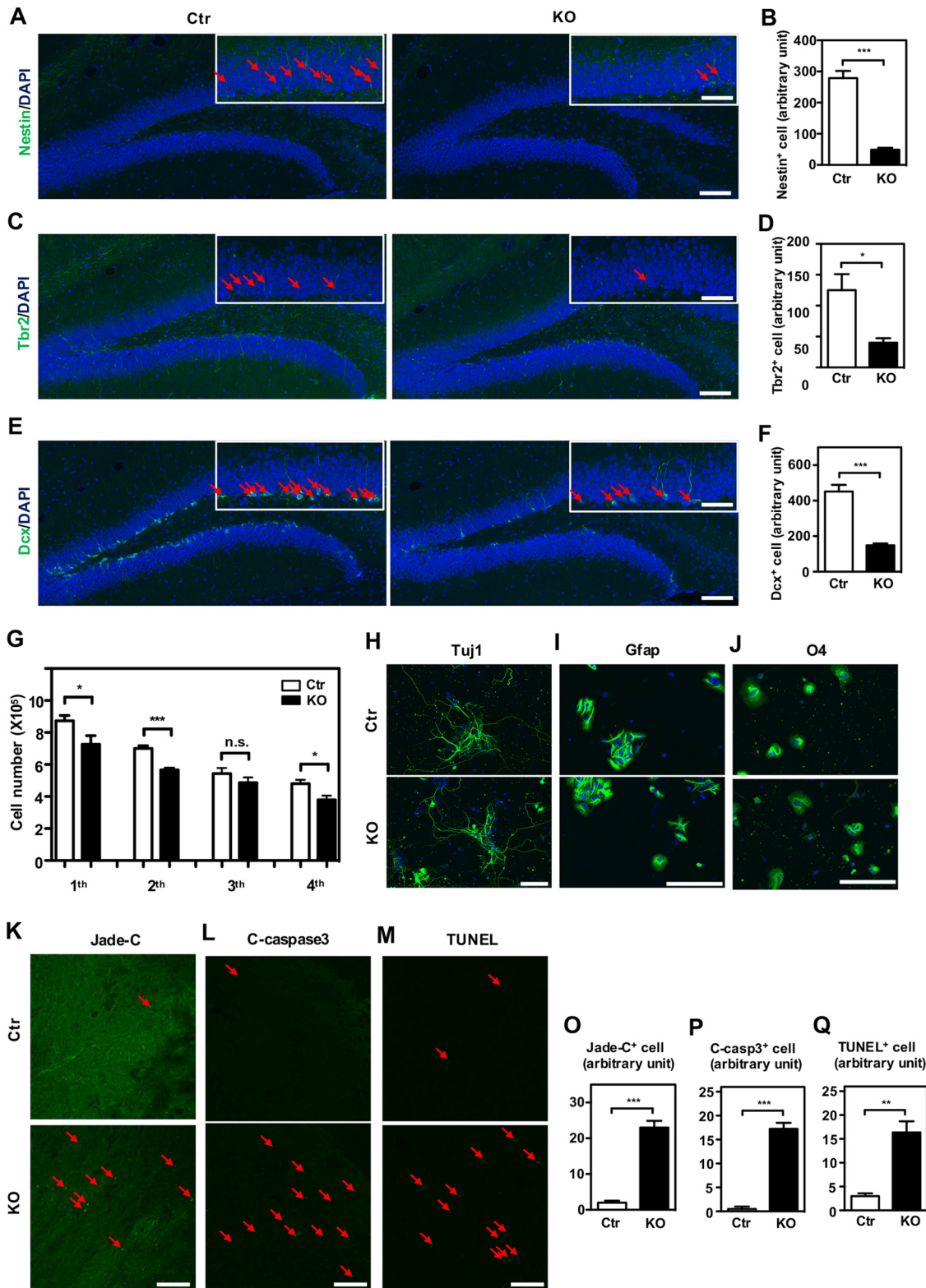


FIG 6 Deletion of *L2hgdh* results in impaired neurogenesis, neurodegeneration, and cell death. (A) Nestin staining in neural progenitor cells in the adult SGZ. Shown are coronal images of the SGZ in 2-month-old *L2hgdh* KO and wild-type mice. Their density is quantified in panel B. (C and D) Reduction of Tbr2⁺ intermediate progenitors in 2-month-old *L2hgdh* KO mouse brains compared to controls. (E and F) Reduction of newborn neurons represented by Dcx⁺ cells in 2-month-old *L2hgdh* KO compared to control mouse brains. The scale bars for panels A, C, and E at the lower right are 100 μ m, and the upper right insets are enlarged images with a scale bar of 50 μ m. (G) *L2hgdh* KO reduces the self-renewal of neural progenitor cells *in vitro*. Neural progenitor cells were isolated from the hippocampus and cultured for four generations, with an initial seeding density of 50,000 cells/well. (H to J) The tripotent differentiation capacity of *L2hgdh* KO neural progenitor cells. Neural progenitor cells isolated from the hippocampus of *L2hgdh* KO and wild-type mice (Continued on next page)

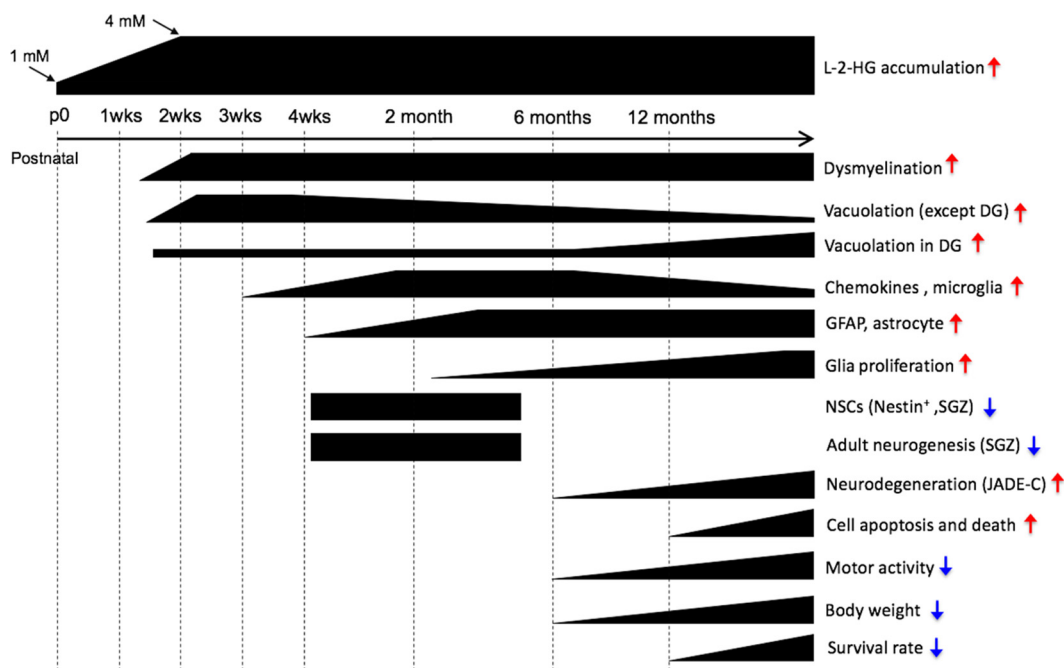


FIG 7 Schematic illustration of disease onset in *L2ghdh* KO mice. The red arrows indicate activation or increase, while blue arrows indicate inactivation or reduction.

might be a compensatory effect in response to reduced myelination. L-2-HG accumulation may compromise the maintenance of the neural progenitor pool, leading to reduced neurogenesis without affecting the tripotent differentiation potential of NPCs *in vitro*. The long-term burden of high L-2-HG levels could further induce apoptosis and neurodegeneration, eventually leading to decreased motor activity, reduced body weight, and death.

Our current study is in line with previous work conducted by Rzem et al., demonstrating that L-2-HG accumulates most significantly in the brain and testis of *L2ghdh* KO mice (21). We further show that high L-2-HG burden led to epigenetic disruption and progressive atrophy of the testis. In previous studies, *L2ghdh* KO mice exhibit increased distance of movement in OFT; however, this was not observed in our current study. This may be due to age differences of mice used for comparison, as we also observed increased motor activity in younger mice (data not shown). We speculate that the long-term burden of high L-2-HG could severely compromise motor activity, as most *L2ghdh* KO mice older than 8 months completely lost movement under routine feeding conditions. Moreover, this is in line with clinical reports that L-2-HGA patients exhibit delayed motor development, frequently accompanied by loss of milestones like unassisted walking (2).

Both dys/demyelination and vacuolation occur during the second week after birth in the *L2ghdh* KO mice. This time point closely correlates with the peak accumulation of L-2-HG. Considering that most peripheral tissues contain less than 1 mM L2-HG and are quite normal in *L2ghdh* KO mice, intracellular L-2-HG levels may need to reach a higher level (i.e., >1 mM) to cause pathological changes. Postnatal week 2 is crucial for CNS pathology in *L2ghdh* KO mice, as it is a critical time point for OPC differentiation, oligodendrocyte maturation, and axon myelination in the mouse brain (42, 43). Myeli-

FIG 6 Legend (Continued)

were induced to differentiate into neurons, astrocytes, and oligodendrocytes *in vitro*. Scale bars for panels H to J are 100 μ m. (K to Q) Neurodegeneration caused by *L2ghdh* KO in the CNS. Serial coronal sections from 14-month-old *L2ghdh* KO and wild-type mice were used for Fluoro Jade-C staining (K), cleaved caspase 3 (L), and TUNEL staining (M). Representative images of the globus pallidus are shown. The scale bar is 100 μ m. (O to Q) Respective quantifications of data from panels K to M. Quantifications are presented as means \pm SEM and were analyzed by a two-tailed *t* test. ***, $P < 0.001$; **, $P < 0.01$; *, $P < 0.05$; n.s., not significant.

nation is relatively normal at postnatal day 9 but the deficiency occurs around postnatal day 12, suggesting that early development, differentiation, and maturation of oligodendrocytes are normal. It is possible that L-2-HG affects mostly the later stages of oligodendrocyte maturation and myelination.

Vacuolation of the CNS is a common feature in mice with high levels of either L-2-HG or D-2-HG, as this phenotype is also observed in mutant IDH2-R140Q or IDH2-R172K knock-in mice, which accumulate D-2-HG (44). We speculate that neuroinflammation and microglia activation are a host defense reaction against vacuolation for the following reasons: (i) the vacuolation appears earlier and is followed by neuroinflammation and microglia activation; (ii) the activated microglia are recruited and highly proliferative around the vacuolation region in corpus callosum (cc) and myelin fiber of striatum (CPu); (iii) when mice are older than 1 year, the vacuolation phenotype becomes less severe. Concomitantly, the neuroinflammation and microglia activation are diminished.

The alpha-KG-dependent dioxygenase family consists of more than 60 members, and they catalyze hydroxylation reactions on diverse substrates, including histone and DNA demethylation (18). Both D-2-HG and L-2-HG are structurally similar to alpha-KG and have been shown to inhibit dioxygenases (13, 17, 45). Although L-2-HG is more potent than D-2-HG in inhibiting these enzymes, not every alpha-KG-dependent dioxygenase exhibits the same sensitivity to D-2-HG or L-2-HG. In fact, L-2-HG inhibits different dioxygenases with a wide range of potencies *in vitro* (17). The enzymes with the lowest 50% inhibitory concentrations (IC_{50} s) were histone demethylases KDM4A/JMJD2A (IC_{50} of $26 \pm 3 \mu\text{M}$) for H3K9 and H3K36, KDM4C/JMJD2C (IC_{50} of $97 \pm 24 \mu\text{M}$) for H3K9 and H3K36, and KDM2A/FBXL11 (IC_{50} of $48 \pm 15 \mu\text{M}$) for H3K36. In contrast, the enzyme PHD2, which is responsible for Hif-1 α hydroxylation and ubiquitination-mediated degradation, has a relatively high IC_{50} of $419 \pm 150 \mu\text{M}$ (17). As a competitive inhibitor, the IC_{50} of L-2-HG depends on the concentration of alpha-KG and other cosubstrates used in the enzymatic assays. Therefore, we take caution in comparing the *in vitro* IC_{50} and *in vivo* effectiveness of L-2-HG in dioxygenase inhibition. In the *L2hgdh* KO mice, neither ER stress nor a global increase of Hif-1 α was detected. These phenotypes are different from those of the *IDH1-R132H* knock-in mice (29). Interestingly, a significant increase in global methylation of H3K9, H3K27, and H3K36, but not H3K4 or H3K79, was found in the brain and testis, two regions with the highest L-2-HG accumulation in *L2hgdh* KO mice. We speculate that the L-2-HG accumulated in the brain and testis of *L2hgdh* KO mice selectively inhibits some members of the JmjC domain-containing histone demethylases.

Both L-2-HG and D-2-HG are normal metabolic by-products (46). Their intracellular levels in most normal cells and tissues are maintained at low levels through the actions of L2HGDH and D2HGDH (5, 47, 48). Currently, few physiological roles have been associated with either enantiomer of 2-HG. High levels of 2-HG have been implicated in pathogenesis of acidurias, as found in the patients with mutations in *L2HGDH* or *D2HGDH*. Moreover, D-2-HG acts as an oncometabolite in various human cancers harboring mutations in *IDH1* or *IDH2*. Approximately 80% of secondary glioblastomas, 20% of AML, 50% of chondrosarcomas, and 10 to 20% of cholangiocarcinomas accumulate high levels of D-2-HG due to *IDH1* or *IDH2* mutations (49–54). Furthermore, L-2-HG is elevated in clear cell renal cell carcinoma (ccRCC) due to reduced expression of the *L2HGDH* gene. In line with the oncogenic function of 2HG, we found a massive expansion of OPCs in *L2hgdh* KO mice, suggesting a neoplastic effect of L-2-HG. However, no brain malignancy was found in the *L2hgdh* KO mice, indicating that accumulation of L-2-HG alone is insufficient to induce glioma in mice.

L2hgdh KO mice display deficiencies in adult neurogenesis; a similar phenotype has also been observed in *Tet1* deletion mice (55). *Tet1* is highly expressed in the CNS and plays an important role in DNA demethylation (55, 56). In *Tet1*-deficient mice, hypermethylation and reduced expression are observed in genes involved in neuronal progenitor proliferation (55). Similar to the *Tet1* KO mice, neural progenitor cells (NPCs) isolated from the hippocampus of *L2hgdh* KO mice showed reduced capacity for self-renewal; however, this reduction was modest and may not explain the dramatic

reduction in neurogenesis *in vivo*. Additional causes, such as increased apoptosis, were observed in the *L2hgdh* KO brain and may contribute to the neurogenesis defects in the *L2hgdh* mice. The *L2hgdh* KO mice presented in this report provide a valuable model for studying the role of L-2HG in the pathophysiology of human diseases.

MATERIALS AND METHODS

Mice and ethics statement. FVB background *L2hgdh* knockout (KO) mice (*L2hgdh*^{-/-}) were generated by the Institute of Developmental Biology and Molecular Medicine (IDM) at Fudan University using the piggyBac transposon insertion method. Briefly, a modified piggyBac transposon harboring the red fluorescent protein (RFP) gene was inserted between exon 1 and exon 2 of the *L2hgdh* allele. The genomic insertion site is chr12:70798148, and the corresponding insertion DNA sequence is 5'-AATT GTGATTCAAAAATAACATTTCCAGGAATGGAAGCTATACTATGTTATAAAAATGCAAAAGCAAGATAGCAAGA TACCTCTGTAACCTGGTCCGCTTGGCGTTTGTATTGGATAGTTGTTGCTGTGAGGCC-3'. The underlined sequence, AATT, is the insertion site. Knockout efficiency was confirmed by genomic PCR, protein Western blotting, and accumulation of the L2HGDH substrate L-2-hydroxyglutarate. Whole-body *p53* KO mice (B6.129-*Trp53*^{tm1Srcmo}) were purchased from Shanghai Biomodel Organism and verified by genomic PCR. *Trp53*^{+/tm1Srcmo} mice were crossed with *L2hgdh*^{+/-} mice to produce double heterozygous mice (F1). The F1 mice were then intercrossed to produce double-gene-knockout mice and the corresponding control mice with *Trp53* knockout and wild-type *L2hgdh*.

For all of the following experiments, littermate mice were used unless stated otherwise. Mice were bred under standard husbandry conditions at the Fudan University mouse facility on a 12-h light/dark cycle, and all experiments were performed in accordance with the Animal Care and Use Committee at Fudan University.

Neural stem cell assay. Hippocampus cells were dissected from neonatal mouse brain, dissociated using a cell dissociation reagent (A1110501; Thermo), and filtered through a 40- μ m cell filter (Falcon). Cells were quantified by hemocytometer and plated on 6-well ultralow attachment plates (CLS3471-24EA; Corning) at a density of 50,000 cells/well to form neurospheres. The cell growth medium consisted of Dulbecco's modified Eagle's medium nutrient mixture F-12 (10565-018; Thermo) supplemented with N-2 supplement (17502-048; Thermo), B27 supplement minus vitamin A (12587-010; Thermo), epidermal growth factor (EGF; PHG0311; Thermo), fibroblast growth factor (FGF)-basic (PHG0026; Thermo), and penicillin-streptomycin (15070-063; Thermo). Cultured neurospheres were cultured for 7 days before dissociation for cell counting. The tissue/neurosphere dissociation was continued for 4 passages and labeled as primary passage (1st), secondary passage (2nd), 3rd passage, and 4th passage.

The *in vitro* differentiation of neural stem cells was performed with NeuroCult differentiation medium (05704; Stem Cell). Briefly, neurospheres from secondary passage at day 3 to ~5 were dissociated to single cells and plated onto 8-well glass chambers (154941; Nunc) in differentiation medium. After a 7-day culture, cells were fixed and used for immunostaining.

TEM analysis. For TEM, mice were perfused sequentially with phosphate-buffered saline (PBS) and prewarmed 2% glutaraldehyde–2% paraformaldehyde (PFA) in PBS. After perfusion, tissues were fixed overnight and coronally sectioned at 100- μ m thickness by a vibratome (VT1200S; Leica). Tissues were then fixed in OsO₄ for 1 h and embedded in epoxy resin. Ultrathin sections were cut with a diamond knife to 75 nm (EM UC6; Leica) and visualized using TEM (JEM-1230; JEOL).

SRS analysis. Details for the SRS microscope setup were described previously (31, 32).

OFT. The OFT comprehensively assessed behavioral and locomotor activity levels of rodents, which can be correlated with locomotive function. Briefly, each mouse was dropped in the same place of a square arena (60-cm length) and video tracked for 10 min. The total distance of movement was measured and quantified automatically.

Antibodies. Antibodies against *L2hgdh* (15707-1-AP; Proteintech), beta-actin (A00702; GenScript), Hif-1 α (610958; BD), eIF2 α (9722; CST), and phospho-eIF2 α (Ser51) (9721; CST) were used for Western blotting. Gfap (MAB360; Millipore), Iba1 (019-441; Wako), Olig2 (AB9610; Millipore), Ng2 (AB53320; Millipore), CC-1 (OP80-100UGCN; Millipore), collagen type IV (600-401-106; Rockland), Cd68 (14-0681-80; eBioscience), nestin (MAB2736; R&D), Tbr2 (ab23345 Abcam), doublecortin (Dcx) (sc-241380; Santa Cruz), and cleaved caspase-3 (Asp175) (5A1E) (CST 9664) were used for immunofluorescence or immunohistochemistry.

Western blotting. Mouse tissues were lysed in radioimmunoprecipitation assay (RIPA) buffer supplemented with a cocktail of protease inhibitors. Proteins were blotted by following standard protocols.

Tissue preparation and histology analysis. Frozen and paraffin-embedded sections were utilized for histological analysis. Wild-type and KO littermates were perfused with PBS and then 4% PFA in PBS at various time points. For frozen sections, brains were fixed in 4% PFA overnight at 4°C and transferred sequentially to 15% and then 30% sucrose after the brain sank to the bottom. Brains were embedded and frozen in OCT compound (Tissue-Tek), and 40- μ m serial sections were coronally prepared by frozen microtome (CM1950; Leica). For paraffin-embedded sections, postfixed brains were sagittally or coronally prepared at 4- μ m thickness. Slides from histologically comparable positions were picked for immunohistochemistry or immunofluorescence staining. To visualize myelinated fibers, frozen sections of brain tissue were processed using Luxol fast blue staining (S3382; Sigma) or FluoroMyelin fluorescent myelin staining (F34651; Thermo) according to standard protocols. For hematoxylin-eosin (HE) staining, paraffin-embedded tissue sections (4 μ m) were used. To identify degenerating neurons, Fluoro-Jade C histofluorescent staining was performed according to the manufacturer's protocol (AG325-30MG; Millipore).

IHC, IF, and confocal imaging. Immunocytochemistry (IHC) and immunofluorescence (IF) were performed on paraffin sections and frozen sections, respectively. Visualization of primary antibodies was performed by the avidin-biotin-horseradish peroxidase system for IHC and Alexa Fluor 488/647-conjugated secondary antibodies (Invitrogen) for IF. The primary antibodies used in this study are listed in “Antibodies,” above. Sections were visualized under a fluorescence laser scanning confocal microscope (A1; Nikon).

Whole-body fat composition analysis. The fat composition of mice was measured nondestructively by Bruker’s minispec whole-body composition analyzer by following the manufacturer’s instructions. The method is based on time domain nuclear magnetic resonance (TD-NMR).

MRI analysis. We carried out T2-weighted MRI *in vivo* at 7.0 T using a Bruker BioSpin MRI GmbH system according to standard procedures.

Metabolite extraction and GC-MS analysis. The GC-MS analysis was performed as previously described (45). Standard curves of commercial L-2-HG and creatinine were used to quantify L-2-HG and creatinine in the samples.

Measurement of GSSG and GSH levels. Oxidized glutathione (GSSG) and reduced glutathione (GSH) levels were determined by using liquid chromatography-tandem mass spectrometry (LC-MS/MS). Briefly, tissues were homogenized by using 10-fold 80% (vol/vol) chilled methanol and then centrifuged at 12,000 rpm for 10 min at 4°C. The supernatant then was subjected to LC-MS/MS analysis using a Shimadzu LC system coupled with a 4000-qtrap triple-quadrupole mass spectrometer (AB Sciex). A Phenomenex NH2 column (inner diameter, 50 mm by 2.0 mm; particle size, 5 μ m) was used. The mass spectrometer was optimized and set up in selected reaction monitoring (SRM) scan mode for monitoring the [M-H] of GSSG (m/z 611.6 \rightarrow 306.2) and GSH (m/z 306.2 \rightarrow 142.8). Analyst software was used for analysis.

RNA isolation and qRT-PCR analysis. Total RNA was isolated from specific brain regions using TransZol Up (TransGen) by following the manufacturer’s instructions. RNA was reverse transcribed with random primer (N9) (TransGen) and proceeded to qRT-PCR with gene-specific primers by SYBR Premix EX tag (TaKaRa). The relative expression abundance of specific genes was calculated by normalization to the beta-actin control. Primer sequences can be provided upon request.

Quantitative analysis of 5mC and its derivatives. Quantification of genomic cytosine and its derivatives was performed by LC-MS/MS as previously described (57).

Gene expression analysis. Next-generation sequencing was performed using standard methods. Briefly, total RNA was extracted using TransZol Up (TransGen). Samples were quantified with an Agilent 2100 Bioanalyzer. Library preparation and RNA sequencing were conducted using TruSeq and a HiSeq 2500 platform (Illumina Inc., San Diego, CA) at WuXi AppTec (Shanghai, China).

For sequencing result analysis, paired-end reads were aligned to the mouse genome (mm9) after quality filtering using Mapsplice, and we performed the quantitation with RSEM. Hierarchical clustering was performed with the open-source application Cluster 3.0 and visualized with Java TreeView. The differential expression analysis was carried out using DESeq2. We performed GO analysis with iPathwayGuide.

Histone methylation profiling. Histone methylation was quantified by MRM-based LC-MS/MS (LC-MRM-MS), as described previously (23, 24). In short, the core histones were acid extracted from tissue with 0.4 M H₂SO₄ and precipitated with trichloroacetic acid (TCA), followed by 2 washes with ice-cold acetone. The histones were treated with *N*-hydroxysuccinimide-propionate and digested with trypsin. Finally, the digested peptides were concentrated to dryness. Prior to LC-MRM-MS, a mixture of isotope-labeled histone peptides was added as internal standards to the samples, and the histone peptide concentration in the samples was calculated by the peak area ratio of histone peptides to internal standard peptides.

Statistical methods. Results are presented as means \pm standard errors of the means (SEM) unless otherwise specified. Statistical analysis was performed using two-tailed unpaired Student’s *t* test. *P* values less than 0.05 were considered significant.

Accession number(s). The full data set has been deposited in the GEO public database under accession number [GSE89806](https://www.ncbi.nlm.nih.gov/geo/query/acc.cgi?acc=GSE89806).

SUPPLEMENTAL MATERIAL

Supplemental material for this article may be found at <https://doi.org/10.1128/MCB.00492-16>.

FIG S1, PDF file, 7.1 MB.

TABLE S1, XLSX file, 0.1 MB.

ACKNOWLEDGMENTS

We thank members of the Fudan MCB laboratory for their valuable inputs and support throughout this study and Jian Hu, Yuan Zhu, and Vivian Fu for critical discussion and reading of the manuscript.

This work was supported by the CAS Strategic Priority Research Program (XDB02050400), NSFC grants (91432111) to Z.Q., by the 973 Program (no. 2012CB910303 to D.Y. and no. 2012CB910101 to K.-L.G.), the NSFC grant (no. 81372198 and no. 81522033 to D.Y.), the NSFC Program of International Cooperation and Exchanges (no. 81120108016 to Y.X.), and the Shanghai “Phosphor” Science Foundation, China (no. 14QA1400600 to D.Y.).

This work was also supported by NIH grants (GM067113 and CA1638311 to Y.X.; CA196878 and GM51586 to K.-L.G.).

REFERENCES

1. Steenweg ME, Jakobs C, Errami A, van Dooren SJ, Adeva Bartolome MT, Aerssens P, Augoustides-Savvopoulou P, Baric I, Baumann M, Bonafe L, Chabrol B, Clarke JT, Clayton P, Coker M, Cooper S, Falik-Zaccari T, Gorman M, Hahn A, Hasanoglu A, King MD, de Klerk HB, Korman SH, Lee C, Meldgaard Lund A, Mejaski-Bosnjak V, Pascual-Castroviejo I, Raadhyaksha A, Rootwelt T, Roubertie A, Ruiz-Falco ML, Scalais E, Schimmel U, Seijo-Martinez M, Suri M, Sykut-Cegielska J, Trefz FK, Uziel G, Valayannopoulos V, Vianey-Saban C, Vlaho S, Vodopituz J, Wajner M, Walter J, Walter-Derbort C, Yapici Z, Zafeiriou DI, Spreuuenberg MD, Celli J, den Dunnen JT, van der Knaap MS, Salomons GS. 2010. An overview of L-2-hydroxyglutarate dehydrogenase gene (L2HGDH) variants: a genotype-phenotype study. *Hum Mutat* 31:380–390. <https://doi.org/10.1002/humu.21197>.
2. Kranendijk M, Struys EA, Salomons GS, Van der Knaap MS, Jakobs C. 2012. Progress in understanding 2-hydroxyglutaric acidurias. *J Inher Metab Dis* 35:571–587. <https://doi.org/10.1007/s10545-012-9462-5>.
3. Sasaki M, Knobbe CB, Munger JC, Lind EF, Brenner D, Brustle A, Harris IS, Holmes R, Wakeham A, Haight J, You-Ten A, Li WY, Schalm S, Su SM, Virtanen C, Reifenberger G, Ohashi PS, Barber DL, Figueroa ME, Melnick A, Zuniga-Pflucker JC, Mak TW. 2012. IDH1(R132H) mutation increases murine haematopoietic progenitors and alters epigenetics. *Nature* 488: 656–659. <https://doi.org/10.1038/nature11323>.
4. Kranendijk M, Struys EA, van Schaftingen E, Gibson KM, Kanhai WA, van der Knaap MS, Amiel J, Buist NR, Das AM, de Klerk JB, Feigenbaum AS, Grange DK, Hofstede FC, Holme E, Kirk EP, Korman SH, Morava E, Morris A, Smeitink J, Sukhai RN, Vallance H, Jakobs C, Salomons GS. 2010. IDH2 mutations in patients with D-2-hydroxyglutaric aciduria. *Science* 330: 336. <https://doi.org/10.1126/science.1192632>.
5. Achouri Y, Noel G, Vertommen D, Rider MH, Veiga-Da-Cunha M, Van Schaftingen E. 2004. Identification of a dehydrogenase acting on D-2-hydroxyglutarate. *Biochem J* 381:35–42. <https://doi.org/10.1042/BJ20031933>.
6. Kranendijk M, Struys EA, Gibson KM, Wickenhagen WV, Abdenur JE, Buechner J, Christensen E, de Kremer RD, Errami A, Gissen P, Gradowska W, Hobson E, Islam L, Korman SH, Kurczynski T, Maranda B, Meli C, Rizzo C, Sansaricq C, Trefz FK, Webster R, Jakobs C, Salomons GS. 2010. Evidence for genetic heterogeneity in D-2-hydroxyglutaric aciduria. *Hum Mutat* 31:279–283. <https://doi.org/10.1002/humu.21186>.
7. Wickenhagen WV, Salomons GS, Gibson KM, Jakobs C, Struys EA. 2009. Measurement of D-2-hydroxyglutarate dehydrogenase activity in cell homogenates derived from D-2-hydroxyglutaric aciduria patients. *J Inher Metab Dis* 32:264–268. <https://doi.org/10.1007/s10545-009-1104-1>.
8. Moroni I, Bugiani M, D'Incerti L, Maccagnano C, Rimoldi M, Bissola L, Pollo B, Finocchiaro G, Uziel G. 2004. L-2-hydroxyglutaric aciduria and brain malignant tumors: a predisposing condition? *Neurology* 62: 1882–1884. <https://doi.org/10.1212/01.WNL.0000125335.21381.87>.
9. Aghili M, Zahedi F, Rafiee E. 2009. Hydroxyglutaric aciduria and malignant brain tumor: a case report and literature review. *J Neurooncol* 91:233–236. <https://doi.org/10.1007/s11060-008-9706-2>.
10. Haliloglu G, Jobard F, Oguz KK, Anlar B, Akalan N, Coskun T, Sass JO, Fischer J, Topcu M. 2008. L-2-hydroxyglutaric aciduria and brain tumors in children with mutations in the L2HGDH gene: neuroimaging findings. *Neuropediatrics* 39:119–122. <https://doi.org/10.1055/s-2008-1081217>.
11. Fu X, Chin RM, Vergnes L, Hwang H, Deng G, Xing Y, Pai MY, Li S, Ta L, Fazlollahi F, Chen C, Prins RM, Teitell MA, Nathanson DA, Lai A, Faull KF, Jiang M, Clarke SG, Cloughesy TF, Graeber TG, Braas D, Christofk HR, Jung ME, Reue K, Huang J. 2015. 2-Hydroxyglutarate inhibits ATP synthase and mTOR signaling. *Cell Metab* 22:508–515. <https://doi.org/10.1016/j.cmet.2015.06.009>.
12. Chan SM, Thomas D, Corces-Zimmerman MR, Xavy S, Rastogi S, Hong WJ, Zhao F, Medeiros BC, Tyvoll DA, Majeti R. 2015. Isocitrate dehydrogenase 1 and 2 mutations induce BCL-2 dependence in acute myeloid leukemia. *Nat Med* 21:178–184. <https://doi.org/10.1038/nm.3788>.
13. Xu W, Yang H, Liu Y, Yang Y, Wang P, Kim SH, Ito S, Yang C, Wang P, Xiao MT, Liu LX, Jiang WQ, Liu J, Zhang JY, Wang B, Frye S, Zhang Y, Xu YH, Lei QY, Guan KL, Zhao SM, Xiong Y. 2011. Oncometabolite 2-hydroxyglutarate is a competitive inhibitor of alpha-ketoglutarate-dependent dioxygenases. *Cancer Cell* 19:17–30. <https://doi.org/10.1016/j.ccr.2010.12.014>.
14. Ye D, Ma S, Xiong Y, Guan KL. 2013. R-2-hydroxyglutarate as the key effector of IDH mutations promoting oncogenesis. *Cancer Cell* 23: 274–276. <https://doi.org/10.1016/j.ccr.2013.03.005>.
15. Shim EH, Livi CB, Rakheja D, Tan J, Benson D, Parekh V, Kho EY, Ghosh AP, Kirkman R, Velu S, Dutta S, Chenna B, Rea SL, Mishur RJ, Li Q, Johnson-Pais TL, Guo L, Bae S, Wei S, Block K, Sudarshan S. 2014. L-2-hydroxyglutarate: an epigenetic modifier and putative oncometabolite in renal cancer. *Cancer Discov* 4:1290–1298. <https://doi.org/10.1158/2159-8290.CD-13-0696>.
16. Losman JA, Looper RE, Koivunen P, Lee S, Schneider RK, McMahon C, Cowley GS, Root DE, Ebert BL, Kaelin WG, Jr. 2013. (R)-2-hydroxyglutarate is sufficient to promote leukemogenesis and its effects are reversible. *Science* 339:1621–1625. <https://doi.org/10.1126/science.1231677>.
17. Chowdhury R, Yeoh KK, Tian YM, Hillringhaus L, Bagg EA, Rose NR, Leung IK, Li XS, Woon EC, Yang M, McDonough MA, King ON, Clifton IJ, Klose RJ, Claridge TD, Ratcliffe PJ, Schofield CJ, Kawamura A. 2011. The oncometabolite 2-hydroxyglutarate inhibits histone lysine demethylases. *EMBO Rep* 12:463–469. <https://doi.org/10.1038/embor.2011.43>.
18. Loenarz C, Schofield CJ. 2008. Expanding chemical biology of 2-oxoglutarate oxygenases. *Nat Chem Biol* 4:152–156. <https://doi.org/10.1038/nchembio0308-152>.
19. Koivunen P, Lee S, Duncan CG, Lopez G, Lu G, Ramkissoon S, Losman JA, Joensuu P, Bergmann U, Gross S, Travins J, Weiss S, Looper R, Ligon KL, Verhaak RG, Yan H, Kaelin WG, Jr. 2012. Transformation by the (R)-enantiomer of 2-hydroxyglutarate linked to EGLN activation. *Nature* 483:484–488. <https://doi.org/10.1038/nature10898>.
20. Van Schaftingen E, Rzem R, Veiga-da-Cunha M. 2009. L-2-hydroxyglutaric aciduria, a disorder of metabolite repair. *J Inher Metab Dis* 32:135–142. <https://doi.org/10.1007/s10545-008-1042-3>.
21. Rzem R, Achouri Y, Marbaix E, Schakman O, Wiame E, Marie S, Gailly P, Vincent MF, Veiga-da-Cunha M, Van Schaftingen E. 2015. A mouse model of L-2-hydroxyglutaric aciduria, a disorder of metabolite repair. *PLoS One* 10:e0119540. <https://doi.org/10.1371/journal.pone.0119540>.
22. Wang P, Wu J, Ma S, Zhang L, Yao J, Hoedley KA, Wilkerson MD, Perou CM, Guan KL, Ye D, Xiong Y. 2015. Oncometabolite D-2-hydroxyglutarate inhibits ALKBH DNA repair enzymes and sensitizes IDH mutant cells to alkylating agents. *Cell Rep* 13:2353–2361. <https://doi.org/10.1016/j.celrep.2015.11.029>.
23. Gao J, Liao R, Yu Y, Zhai H, Wang Y, Sack R, Peters AH, Chen J, Wu H, Huang Z, Hu M, Qi W, Lu C, Atadja P, Oyang C, Li E, Yi W, Zhou S. 2014. Absolute quantification of histone PTM marks by MRM-based LC-MS/MS. *Anal Chem* 86:9679–9686. <https://doi.org/10.1021/ac502333a>.
24. Yu Y, Chen J, Gao Y, Gao J, Liao R, Wang Y, Oyang C, Li E, Zeng C, Zhou S, Yang P, Jin H, Yi W. 2016. Quantitative profiling of combinatorial K27/K36 modifications on histone H3 variants in mouse organs. *J Proteome Res* 15:1070–1079. <https://doi.org/10.1021/acs.jproteome.5b01164>.
25. Figueroa ME, Abdel-Wahab O, Lu C, Ward PS, Patel J, Shih A, Li Y, Bhagwat N, Vasanthakumar A, Fernandez HF, Tallman MS, Sun Z, Wolniak K, Peeters JK, Liu W, Choe SE, Fantin VR, Paietta E, Lowenberg B, Licht JD, Godley LA, Delwel R, Valk PJ, Thompson CB, Levine RL, Melnick A. 2010. Leukemic IDH1 and IDH2 mutations result in a hypermethylation phenotype, disrupt TET2 function, and impair hematopoietic differentiation. *Cancer Cell* 18:553–567. <https://doi.org/10.1016/j.ccr.2010.11.015>.
26. He YF, Li BZ, Li Z, Liu P, Wang Y, Tang Q, Ding J, Jia Y, Chen Z, Li L, Sun Y, Li X, Dai Q, Song CX, Zhang K, He C, Xu GL. 2011. Tet-mediated formation of 5-carboxylcytosine and its excision by TDG in mammalian DNA. *Science* 333:1303–1307. <https://doi.org/10.1126/science.1210944>.
27. Ito S, Shen L, Dai Q, Wu SC, Collins LB, Swenberg JA, He C, Zhang Y. 2011. Tet proteins can convert 5-methylcytosine to 5-formylcytosine and 5-carboxylcytosine. *Science* 333:1300–1303. <https://doi.org/10.1126/science.1210597>.
28. Tahiliani M, Koh KP, Shen Y, Pastor WA, Bandukwala H, Brudno Y, Agarwal S, Iyer LM, Liu DR, Aravind L, Rao A. 2009. Conversion of 5-methylcytosine to 5-hydroxymethylcytosine in mammalian DNA by MLL partner TET1. *Science* 324:930–935. <https://doi.org/10.1126/science.1170116>.
29. Sasaki M, Knobbe CB, Itsumi M, Elia AJ, Harris IS, Chio II, Cairns RA, McCracken S, Wakeham A, Haight J, Ten AY, Snow B, Ueda T, Inoue S, Yamamoto K, Ko M, Rao A, Yen KE, Su SM, Mak TW. 2012. D-2-

- hydroxyglutarate produced by mutant IDH1 perturbs collagen maturation and basement membrane function. *Genes Dev* 26:2038–2049. <https://doi.org/10.1101/gad.198200.112>.
30. Steenweg ME, Salomons GS, Yapici Z, Uziel G, Scalais E, Zafeiriou DI, Ruiz-Falco ML, Mejaski-Bosnjak V, Augoustides-Savvopoulou P, Wajner M, Walter J, Verhoeven-Duif NM, Struys EA, Jakobs C, van der Knaap MS. 2009. L-2-hydroxyglutaric aciduria: pattern of MR imaging abnormalities in 56 patients. *Radiology* 251:856–865. <https://doi.org/10.1148/radiol.2513080647>.
 31. Ji M, Orringer DA, Freudiger CW, Ramkissoon S, Liu X, Lau D, Golby AJ, Norton I, Hayashi M, Agar NY, Young GS, Spino C, Santagata S, Camelo-Piragua S, Ligon KL, Sagher O, Xie XS. 2013. Rapid, label-free detection of brain tumors with stimulated Raman scattering microscopy. *Sci Transl Med* 5:201ra119.
 32. Freudiger CW, Min W, Saar BG, Lu S, Holtom GR, He C, Tsai JC, Kang JX, Xie XS. 2008. Label-free biomedical imaging with high sensitivity by stimulated Raman scattering microscopy. *Science* 322:1857–1861. <https://doi.org/10.1126/science.1165758>.
 33. Liu C, Sage JC, Miller MR, Verhaak RG, Hippenmeyer S, Vogel H, Foreman O, Bronson RT, Nishiyama A, Luo L, Zong H. 2011. Mosaic analysis with double markers reveals tumor cell of origin in glioma. *Cell* 146:209–221. <https://doi.org/10.1016/j.cell.2011.06.014>.
 34. Liu C, Zong H. 2012. Developmental origins of brain tumors. *Curr Opin Neurobiol* 22:844–849. <https://doi.org/10.1016/j.conb.2012.04.012>.
 35. Cancer Genome Atlas Research Network, Brat DJ, Verhaak RG, Aldape KD, Yung WK, Salama SR, Cooper LA, Rheinbay E, Miller CR, Vitucci M, Morozova O, Robertson AG, Nouthmehr H, Laird PW, Cherniack AD, Akbani R, Huse JT, Ciriello G, Poisson LM, Barnholtz-Sloan JS, Berger MS, Brennan C, Colen RR, Colman H, Flanders AE, Giannini C, Grifford M, Iavarone A, Jain R, Joseph I, Kim J, Kasaian K, Mikkelsen T, Murray BA, O'Neill BP, Pachter L, Parsons DW, Sougnez C, Sulman EP, Vandenberg SR, Van Meir EG, von Deimling A, Zhang H, Crain D, Lau K, Mallery D, Morris S, Paulauskis J, Penny R, Shelton T, et al. 2015. Comprehensive, integrative genomic analysis of diffuse lower-grade gliomas. *N Engl J Med* 372:2481–2498. <https://doi.org/10.1056/NEJMoa1402121>.
 36. Suzuki H, Aoki K, Chiba K, Sato Y, Shiozawa Y, Shiraishi Y, Shimamura T, Niida A, Motomura K, Ohka F, Yamamoto T, Tanahashi K, Ranjit M, Wakabayashi T, Yoshizato T, Kataoka K, Yoshida K, Nagata Y, Sato-otsubo A, Tanaka H, Sanada M, Kondo Y, Nakamura H, Mizoguchi M, Abe T, Muragaki Y, Watanabe R, Ito I, Miyano S, Natsume A, Ogawa S. 2015. Mutational landscape and clonal architecture in grade II and III gliomas. *Nat Genet* 47:458–468. <https://doi.org/10.1038/ng.3273>.
 37. Kouzarides T. 2002. Histone methylation in transcriptional control. *Curr Opin Genet Dev* 12:198–209. [https://doi.org/10.1016/S0959-437X\(02\)00287-3](https://doi.org/10.1016/S0959-437X(02)00287-3).
 38. Akbarian S, Huang HS. 2009. Epigenetic regulation in human brain-focus on histone lysine methylation. *Biol Psychiatry* 65:198–203. <https://doi.org/10.1016/j.biopsych.2008.08.015>.
 39. Tansey MG, Goldberg MS. 2010. Neuroinflammation in Parkinson's disease: its role in neuronal death and implications for therapeutic intervention. *Neurobiol Dis* 37:510–518. <https://doi.org/10.1016/j.nbd.2009.11.004>.
 40. Minghetti L. 2005. Role of inflammation in neurodegenerative diseases. *Curr Opin Neurol* 18:315–321. <https://doi.org/10.1097/01.wco.0000169752.54191.97>.
 41. Schmued LC, Stowers CC, Scallet AC, Xu L. 2005. Fluoro-Jade C results in ultra high resolution and contrast labeling of degenerating neurons. *Brain Res* 1035:24–31. <https://doi.org/10.1016/j.brainres.2004.11.054>.
 42. Hill RA, Patel KD, Goncalves CM, Grutzendler J, Nishiyama A. 2014. Modulation of oligodendrocyte generation during a critical temporal window after NG2 cell division. *Nat Neurosci* 17:1518–1527. <https://doi.org/10.1038/nn.3815>.
 43. Sauvageot CM, Stiles CD. 2002. Molecular mechanisms controlling cortical gliogenesis. *Curr Opin Neurobiol* 12:244–249. [https://doi.org/10.1016/S0959-4388\(02\)00322-7](https://doi.org/10.1016/S0959-4388(02)00322-7).
 44. Akbay EA, Moslehi J, Christensen CL, Saha S, Tchaicha JH, Ramkissoon SH, Stewart KM, Carretero J, Kikuchi E, Zhang H, Cohoon TJ, Murray S, Liu W, Uno K, Fisch S, Jones K, Gurumurthy S, Gliser C, Choe S, Keenan M, Son J, Stanley I, Losman JA, Padera R, Bronson RT, Asara JM, Abdel-Wahab O, Amrein PC, Fathi AT, Danial NN, Kimmelman AC, Kung AL, Ligon KL, Yen KE, Kaelin WG, Jr, Bardeesy N, Wong KK. 2014. D-2-hydroxyglutarate produced by mutant IDH2 causes cardiomyopathy and neurodegeneration in mice. *Genes Dev* 28:479–490. <https://doi.org/10.1101/gad.231233.113>.
 45. Ma S, Jiang B, Deng W, Gu ZK, Wu FZ, Li T, Xia Y, Yang H, Ye D, Xiong Y, Guan KL. 2015. D-2-hydroxyglutarate is essential for maintaining oncogenic property of mutant IDH-containing cancer cells but dispensable for cell growth. *Oncotarget* 6:8606–8620. <https://doi.org/10.18632/oncotarget.3330>.
 46. Fan J, Teng X, Liu L, Mattaini KR, Looper RE, Vander Heiden MG, Rabinowitz JD. 2015. Human phosphoglycerate dehydrogenase produces the oncometabolite D-2-hydroxyglutarate. *ACS Chem Biol* 10:510–516. <https://doi.org/10.1021/cb500683c>.
 47. Topcu M, Jobard F, Halliez S, Coskun T, Yalcinkaya C, Gerceker FO, Wanders RJ, Prud'homme JF, Lathrop M, Ozguc M, Fischer J. 2004. L-2-hydroxyglutaric aciduria: identification of a mutant gene C14orf160, localized on chromosome 14q22.1. *Hum Mol Genet* 13:2803–2811. <https://doi.org/10.1093/hmg/ddh300>.
 48. Rzem R, Veiga-da-Cunha M, Noel G, Goffette S, Nassogne MC, Tabarki B, Scholler C, Marquardt T, Vikkula M, Van Schaftingen E. 2004. A gene encoding a putative FAD-dependent L-2-hydroxyglutarate dehydrogenase is mutated in L-2-hydroxyglutaric aciduria. *Proc Natl Acad Sci U S A* 101:16849–16854. <https://doi.org/10.1073/pnas.0404840101>.
 49. Parsons DW, Jones S, Zhang X, Lin JC, Leary RJ, Angenendt P, Mankoo P, Carter H, Siu IM, Gallia GL, Olivari A, McLendon R, Rasheed BA, Keir S, Nikolskaya T, Nikolsky Y, Busam DA, Tekleab H, Diaz LA, Jr, Hartigan J, Smith DR, Strausberg RL, Marie SK, Shinjo SM, Yan H, Riggins GJ, Bigner DD, Karchin R, Papadopoulos N, Parmigiani G, Vogelstein B, Velculescu VE, Kinzler KW. 2008. An integrated genomic analysis of human glioblastoma multiforme. *Science* 321:1807–1812. <https://doi.org/10.1126/science.1164382>.
 50. Mardis ER, Ding L, Dooling DJ, Larson DE, McLellan MD, Chen K, Koboldt DC, Fulton RS, Delehaunty KD, McGrath SD, Fulton LA, Locke DP, Magrini VJ, Abbott RM, Vickery TL, Reed JS, Robinson JA, Wylie T, Smith SM, Carmichael L, Eldred JM, Harris CC, Walker J, Peck JB, Du F, Dukes AF, Sanderson GE, Brummett AM, Clark E, McMichael JF, Meyer RJ, Schindler JK, Pohl CS, Wallis JW, Shi X, Lin L, Schmidt H, Tang Y, Haipke K, Wiechert ME, Ivy JV, Kalicki J, Elliott G, Ries RE, Payton JE, Westervelt P, Tomasson MH, Watson MA, Baty J, Heath S, Shannon WD, Nagarajan R, Link DC, Walter MJ, Graubert TA, DiPersio JF, Wilson RK, Ley TJ. 2009. Recurring mutations found by sequencing an acute myeloid leukemia genome. *N Engl J Med* 361:1058–1066. <https://doi.org/10.1056/NEJMoa0903840>.
 51. Pansuriya TC, van Eijk R, d'Adamo P, van Ruler MA, Kuijjer ML, Oosting J, Cleton-Jansen AM, van Oosterwijk JG, Verbeke SL, Meijer D, van Wezel T, Nord KH, Sangiorgi L, Toker B, Liegl-Atzwanger B, San-Julian M, Sciort R, Limaye N, Kindblom LG, Daugaard S, Godfraind C, Boon LM, Vikkula M, Kurek KC, Szuhai K, French PJ, Bovee JV. 2011. Somatic mosaic IDH1 and IDH2 mutations are associated with enchondroma and spindle cell hemangioma in Ollier disease and Maffucci syndrome. *Nat Genet* 43:1256–1261. <https://doi.org/10.1038/ng.1004>.
 52. Cairns RA, Iqbal J, Lemonnier F, Kucuk C, de Leval L, Jais JP, Parrens M, Martin A, Xerri L, Brousset P, Chan LC, Chan WC, Gaulard P, Mak TW. 2012. IDH2 mutations are frequent in angioimmunoblastic T-cell lymphoma. *Blood* 119:1901–1903. <https://doi.org/10.1182/blood-2011-11-391748>.
 53. Kipp BR, Voss JS, Kerr SE, Barr Fritcher EG, Graham RP, Zhang L, Highsmith WE, Zhang J, Roberts LR, Gores GJ, Halling KC. 2012. Isocitrate dehydrogenase 1 and 2 mutations in cholangiocarcinoma. *Hum Pathol* 43:1552–1558. <https://doi.org/10.1016/j.humpath.2011.12.007>.
 54. Wang P, Dong Q, Zhang C, Kuan PF, Liu Y, Jeck WR, Andersen JB, Jiang W, Savich GL, Tan TX, Auman JT, Hoskins JM, Misher AD, Moser CD, Yourstone SM, Kim JW, Cibulskis K, Getz G, Hunt HV, Thorgerisson SS, Roberts LR, Ye D, Guan KL, Xiong Y, Qin LX, Chiang DY. 2013. Mutations in isocitrate dehydrogenase 1 and 2 occur frequently in intrahepatic cholangiocarcinomas and share hypermethylation targets with glioblastomas. *Oncogene* 32:3091–3100. <https://doi.org/10.1038/onc.2012.315>.
 55. Zhang RR, Cui QY, Murai K, Lim YC, Smith ZD, Jin S, Ye P, Rosa L, Lee YK, Wu HP, Liu W, Xu ZM, Yang L, Ding YQ, Tang F, Meissner A, Ding C, Shi Y, Xu GL. 2013. Tet1 regulates adult hippocampal neurogenesis and cognition. *Cell Stem Cell* 13:237–245. <https://doi.org/10.1016/j.stem.2013.05.006>.
 56. Guo JU, Su Y, Zhong C, Ming GL, Song H. 2011. Hydroxylation of 5-methylcytosine by TET1 promotes active DNA demethylation in the adult brain. *Cell* 145:423–434. <https://doi.org/10.1016/j.cell.2011.03.022>.
 57. Yang H, Lin H, Xu H, Zhang L, Cheng L, Wen B, Shou J, Guan K, Xiong Y, Ye D. 2014. TET-catalyzed 5-methylcytosine hydroxylation is dynamically regulated by metabolites. *Cell Res* 24:1017–1020. <https://doi.org/10.1038/cr.2014.81>.